

Parameterization of the responses of subarctic European vegetation to key environmental variables for ozone risk assessment

Stefanie Falk^{1,4}, Ane V. Vollsnes², Aud B. Eriksen², Lisa Emberson³, Connie O'Neill³, Frode Stordal¹, and Terje Koren Berntsen¹

¹Department of Geosciences, University of Oslo, Oslo, Norway

²Department of Biosciences, University of Oslo, Oslo, Norway

³Department of Environment and Geography, University of York, UK

⁴Department of Geography, Ludwig Maximilian University of Munich, Munich, Germany

Correspondence: Stefanie Falk (stefanie.falk@lmu.de)

Abstract. The unique vegetation of the subarctic region [1] is adapted to extremes of cold and midnight sun [2] and likely to be at threat from the combined impacts of climate change and increasing ozone concentrations [O₃] [3]. To date, only a few studies [4] assessed the response of subarctic vegetation to variations in [5] climate and air pollution. This study looks to fill this knowledge gap by examining the uncertainty in risk assessments that are [6] using Boreal parameterizations. With no parameterization of stomatal response of subarctic vegetation available [7], we propose an adjustment [8] of existing Boreal parameterizations based on local climate [9] variation. To this end, we vary temperature response functions [10] according to the climatological temperature distribution within the growing season at our site. Thus, we refer to our approach as localization of stomatal response functions. With these, we apply the integrated flux-metric Phytotoxic Ozone Dose (POD) to determine ozone risk and damage to vegetation as a function of [O₃], key environmental variables, and species-specific physiology. In addition, we evaluate the extent to which two recent years (2018 and 2019) deviate from climatic and [O₃] norms and find that 2018 was an anomalously warm and less cloudy year, particularly in spring and early summer. Higher than average [O₃] was observed in April/May while frequent episodes of ozone volume mixing ratios (VMRs) exceeding 40 ppb occurred in June [11]–August. These episodes are in part attributable to forest fires in the Northern Hemisphere and warmer and sunnier conditions. In contrast, 2019 was an average year. Our modeling study suggests that using standard Boreal parameterizations [12] in assessments likely leads to underestimating the risk of ozone damage in this region for some species. We find that localized parameterizations for subarctic vegetation result in an ozone-induced biomass loss of 2.5 to 17.4 %. For some species, this loss is up to 55 % larger than projected from Boreal parameterizations used in general assessments. Efforts should be targeted towards accurately defining subarctic vegetation's physiological response to essential climate variables.

1 Introduction

20 Ground-level ozone (O_3) is a highly toxic pollutant known to cause damage to a variety of ecosystems around the World
(Emberson, 2020). Ozone causes reduced photosynthesis, visible foliar injury, early senescence, and programmed cell death of
plants (Kangaskärvi et al., 2005). Hence affecting the global carbon cycle (Lombardozzi et al., 2013) and crop yields. Annual
global yield losses of four major crops (wheat, rice, maize, and soybean) of 3–15% have been reported (Ainsworth, 2017) and
a suggested loss in primary production in forestry of 7% (Wittig et al., 2009; Matyssek et al., 2012) has been attributed to ozone.
25 Even though long-term (pre-1950) observations of ground-level ozone concentrations are scarce; evidence from trend analysis
of those few sites suggests that since the industrial revolution, background concentrations in the northern hemisphere have at
least doubled and continued to increase (Hartmann et al., 2013) until recently. Recent trend analyses for Europe indicate that a
maximum was reached in 2007 (Derwent et al., 2018), after which tropospheric background ozone started to level off or even
decline (Cooper et al., 2014; Wespes et al., 2018; Gaudel et al., 2018). This can be attributed to a successful implementation of
30 air quality regulations coupled with economic restructuring, reducing the number of episodes of peak concentrations especially
in summertime (e.g., Fleming et al., 2018; Mills et al., 2018). However, changes in environmental conditions associated with
climate change, such as an increase in the frequency of heatwaves, could negate the effectiveness of emission reductions
concerning ozone impacts and air quality (Lin et al., 2020). Tropospheric background ozone concentrations derived from
satellite instruments range between 50–65 ppb over Fennoscandia but strongly depend on season (Cooper et al., 2014).

35 In the annual cycle, a distinct maximum of ground-level ozone concentrations typically occurs in spring followed by lower
concentrations throughout the summer. This ozone spring peak is more pronounced in northern Fennoscandia than in more
southern locations but shows a high interannual variability (Klingberg et al., 2009, 2019). Andersson et al. (2017) showed in
a modeling study focused on Fennoscandia that the variability of ozone concentrations in winter can be mainly attributed to
40 changes in atmospheric background transport of ozone, while summertime abundance is mostly affected by emissions of
precursors in the rest of Europe.

The precursor gases involved in the formation of ground-level ozone are carbon monoxide (CO) and hydrocarbons known as
volatile organic compounds (VOCs) in the presence of nitrogen oxides (NO_x). In northern Fennoscandia, episodes of elevated
summertime ozone concentrations in 2003 and 2006 have been traced back to ozone precursor emissions related to forest fires
in southern and eastern Europe, respectively (Lindskog et al., 2007; Karlsson et al., 2013). Besides VOCs from anthropogenic
45 sources, hydrocarbons are also emitted by photosynthetically active vegetation in the form of terpenes and monoterpenes, so-
called biogenic volatile substances (BVOCs) and soil. These emissions are thought to be a response to factors, such as thermal
stress, defense against herbivores (Ghimire et al., 2021), or even attraction of pollinators (Peñuelas and Llusià, 2003). Ghimire
et al. (2021) found no clear evidence that general warming would increase the BVOC emissions in subarctic vegetation, while
a reduction of herbivory would decrease them by 44–72%.

50 The start of the growing season (GS) in northern Fennoscandia has been shifting to earlier dates in response to the general
warming trend (Menzel et al., 2006; Høgda et al., 2013; Karlsen et al., 2007, e.g.) and thereby converging with the period of the
ozone spring peak. At the same time, the growing season is also becoming longer. A longer growing season is prolonging the



time in which vegetation can accumulate an ozone dose. For natural and semi-natural vegetation that is already subject to rapid climatic changes known as Arctic amplification (AMAP - Arctic Monitoring and Assessment Programme, 2012; Hartmann et al., 2013), these factors could promote a higher potential risk for northern vegetation to ozone-induced damage in the not so distant future. Recently, Hayes et al. (2021) showed that the highest sensitivity to future $[O_3]$ variability is expected in summer when vegetation is most productive.

Ozone acts as oxidative stress to plants. Its main action is imposed through reactions occurring in the cell walls and cell membranes of mesophyll cells inside the leaves. Ozone enters the leaves through stomata, leaf pores that enable gas exchange, allowing the entry of CO_2 for photosynthesis and loss of H_2O vapor via the plant transpiration stream. Stomatal aperture, and hence stomatal conductance to these gases (including ozone) will vary over the day and growing season primarily to balance CO_2 uptake against H_2O vapor loss. The higher the stomatal conductance, the higher the potential for ozone uptake. Stomatal conductance has been empirically linked to key environmental variables such as air temperature T , photosynthetic photon flux density (PPFD), vapor pressure deficit (VPD), and soil water potential (SWP) as well as photosynthesis itself (e.g., Jarvis, 1976; Ball et al., 1987; Emberson et al., 2000; Mills et al., 2017). Results from open-top chamber (OTC) experiments on downy birch (*Betula pubescens*) and mountain birch (*Betula pubescens toruosa*), native to subarctic regions, indicated reductions in both biomass, shoot ratio, and visible leaf damage under elevated ozone treatment ($\chi_{O_3} = 36 - 54$ ppb) (Manninen et al., 2009). Though, Scots pine (*Pinus sylvestris*) is considered to be more ozone tolerant due to absence of visible injuries (Girgždienė et al., 2009), Manninen et al. (2009) found chlorophyll:carotenoid ratio and polyamines reductions under elevated ozone concentrations indicating susceptibility to ozone also in these species.

To estimate the potential ozone risk on subarctic vegetation, we use a flux-based metric, also referred to as the Phytotoxic Ozone Dose over a threshold y (POD_y). Flux-based metrics, that relate the accumulated dose of ozone to a reduction in biomass, are biologically more relevant for risk assessments than exposure-based metrics because they can account for particular species characteristics (i.e. physiology and phenology) as well as key environmental variables that can decouple the relationship between ozone concentration, ozone uptake, and consequent damage (Emberson, 2020). These flux-based metrics are better suited to represent the actual risk to vegetation from ozone, especially in the climatically extreme parts of Europe (Simpson et al., 2007; Mills et al., 2011, 2017). But no bespoke parameterization for subarctic vegetation is available.

The POD_y metric is currently used in risk assessments under the United Nations Economic Commission for Europe (UNECE) Long Range Transboundary Air Pollution (LRTAP) Convention to identify those locations across Europe where vegetation is at risk from ozone. This convention aims to develop an effects-based emission reduction policy that can target those ozone precursor emissions that are most influential in causing damage. To achieve this, the concept of critical levels (CLs) has been adopted and applied (Maas et al., 2016). Exceedance of the CL is used to identify those areas across Europe that would benefit from targeted Europe-wide emission reductions. Methods to estimate POD_y and CLs are defined by the UNECE LRTAP Convention and described in a Mapping Manual (Mills et al., 2017, most recent version). The exceedance of the CL is calculated by:

$$CL_{\text{exceed}} = POD_y - CL. \quad (1)$$

An application of the Mapping Manual method was made by Mills et al. (2011) where exceedance of the CL was related to observations of ozone damage to a clover bio-monitor. This study demonstrated the improved ability of flux-based metrics (in comparison to exposure-based metrics) to identify the geographical distribution of the risk of ozone damage and also showed
90 that the ozone  age could extend into more northerly regions of Europe.

The described methods for risk assessment rely on accurate representation of plant physiological responses to key environmental variables and are most often parameterized using data for less extreme climates, i.e., temperate, continental, or Boreal climates. Parameterization  for more extreme bio-geographical regions such as subarctic climates has not been performed and relies on assuming that less extreme Boreal parameterization will be applicable. It is important to understand the implications of
95 using these in the subarctic. In our study, we explore how risk might be over- or underestimated using  Boreal parameterization and explore an adjustment of temperature  and light response functions based on climate data. This allows an understanding of which are the key aspects of modelled plant physiology that might determine the potential risk and also how the threat from ozone may change in the future. In addition, our results may hint a solution to solve long-standing issues of earth system models (ESM) which often lack PFTs specifically representing subarctic conditions in their land surface models and display
100 over- or underproductivity in the Arctic (Poulter et al., 2015; Lawrence et al., 2019).


In Section 2, we give a brief summary of the key components and drivers of the DO₃SE model that is used to assess the ozone risk. To study the influence of selected parameters on ozone risk in the subarctic, we propose a method to localize temperature response functions based on climate data and to infer start and end of the growing season from satellite observed
105 gross primary productivity (GPP). Results of the ozone risk modelling are presented in Section 3. For evaluating these results, we assess the climate anomaly of weather conditions in the 2018/19 GS at our research site in Section 3.3. In Section 4, we discuss these results concerning prevailing conditions and give an outlook on how future assessments of pollution risk in the subarctic could be improved.

2 Methods

110 In the following, we briefly describe the model used for assessing the ozone risk, its key components, input data, and gap filling procedure (Section 2.1). To study the impact of model parameters, we propose a method for parameter localization to a subarctic climate based on existing Boreal parameterizations and local climate conditions. We estimate the start and end of the growing season from satellite derived GPP (Section 2.2).


2.1 DO3SE model

115 We use the well established Deposition of Ozone for Stomatal Exchange (DO₃SE) model (Büker et al., 2012) which computes estimates of the total and stomatal deposition of O₃ to selected land-cover types and plant species according to UNECE Long-Range Transboundary Air Pollution (LRTAP) methodologies for effects-based risk assessment.


2.1.1 Model description

 An estimate of the stomatal O₃ flux (Φ_{sto}) is calculated based on the assumption that the concentration of O₃ at the top of the canopy h represents a reasonable estimate of the concentration at the upper surface of the laminar layer for a sunlit upper canopy leaf and key environmental variables affecting stomatal conductance. POD_y is then calculated according to:

$$\text{POD}_y = \int (\Phi_{\text{sto}} - y) \cdot dt, \quad (2)$$

with the hourly averaged stomatal ozone flux Φ_{sto} (see Eq. (4)) and a stomatal ozone flux threshold y both given in units of nmol O₃ m⁻² PLA⁻¹ s⁻¹. Herein PLA stands for Projected Leaf Area. The timestep dt is usually 1 hour. The flux threshold y represents the detoxification potential of the plant and is typically only exceeded during daylight hours (i.e. when global radiation is above 50 W m⁻²). POD_y  given in mmol m⁻² integrated over the growing season.

In the DO₃SE model, the stomatal flux Φ_{sto} in Eq. (2) is a fraction of the total O₃ deposition flux. A standard resistance analogous approach (Wesely, 1989) is used to transport O₃ from the atmospheric reference height h_0 to the vegetated surface. The calculation of aerodynamic R_a and quasi-laminar boundary layer resistance R_b follow Simpson et al. (2003, 2012). The surface resistance R_{surf} consists of stomatal r_{sto} and non-stomatal canopy resistances that include external plant surfaces r_{ext} , aerodynamic within-canopy R_{inc} and ground surfaces or soil resistances R_{gs} (Simpson et al., 2003, 2012). Under the assumption that the ozone concentration [O₃] at the top of the canopy represents a reasonable estimate of the concentration at the upper surface of the laminar layer for a sunlit upper canopy leaf, r_{sto} and r_{ext} are calculated per leaf/needle area (note lower case r).

$$R_{\text{sur}} = \frac{1}{\frac{\text{LAI}}{r_{\text{sto}}} + \frac{\text{SAI}}{r_{\text{ext}}} + \frac{1}{R_{\text{inc}} + R_{\text{gs}}}} \quad (3)$$

 Stomatal resistance r_{sto} is the inverse of stomatal conductance g_{sto} in Eq. (5). Accounting for these the effective stomatal flux Φ_{sto} at the vegetation height h is defined as

$$\Phi_{\text{sto}} = [\text{O}_3](h) \cdot g_{\text{sto}}(h). \quad (4)$$

 A linear gradient reducing [O₃] from h_0 to h was adopted in the DO₃SE model based on detailed transport studies using the chemical transport model EMEP (Simpson et al., 2012; Mills et al., 2017).

The opening of stomata referred to as stomatal conductance g_{sto} is governed by different species-specific factors and responds to key environmental variables. In the DO₃SE model, g_{sto} is described by a multiplicative empirical model (Jarvis, 1976; Emberson et al., 2000; Mills et al., 2017):

$$g_{\text{sto}} = g_{\max} \cdot f_{\text{phen}} \cdot f_{\text{light}} \cdot \max \{f_{\min}, f_T \cdot f_{\text{VPD}} \cdot f_{\text{SWP}}\}. \quad (5)$$

Where g_{\max} is a species-specific maximum stomatal conductance value that is modified by factors that vary within a range of 0 – 1. These factors are empirically determined and account for leaf phenology (f_{phen}), light (f_{light}), temperature (f_T), water vapor pressure deficit (f_{VPD}), and soil water potential (f_{SWP}). All factors differ with plant functional type (PFT).

The leaf phenology factor (f_{phen}) is a stepwise defined linear function that allows for increase of stomatal conductance in spring (start of growing season) and a decrease in fall (end of growing season). Mid anthesis and mid season dips in stomata 150 conductance can also be accounted for but are not relevant in this study.

The temperature response function is defined as

$$f_T = \frac{T_{\text{air}} - T_{\min}}{T_{\text{opt}} - T_{\min}} \cdot \left(\frac{T_{\max} - T_{\text{air}}}{T_{\max} - T_{\text{opt}}} \right)^{\beta}, \quad (6)$$

with $\beta = \frac{T_{\max} - T_{\text{opt}}}{T_{\text{opt}} - T_{\min}}$ a mixed reciprocal polynomial function of temperature. The shape parameters T_{\min} , T_{\max} and T_{opt} are tabulated for various PFT and T_{air} is the near-surface air temperature. All temperatures are defined in units of $^{\circ}\text{C}$.

155 The water vapor pressure deficit function is

$$f_{\text{VPD}} = f_{\min} + (1 - f_{\min}) \cdot \frac{D_{\min} - \text{VPD}}{D_{\min} - D_{\max}} \quad (7)$$

where VPD is the leaf to air vapor pressure deficit in kPa with a minimum conductance f_{\min} . D_{\min} , D_{\max} describe the relative stomatal conductance to changes in vapor pressure deficit.

The light response function f_{light} is given by

$$160 \quad f_{\text{light}} = 1 - \exp(-\alpha_{\text{light}} \cdot \text{PPFD}) \quad (8)$$

where α_{light} is a slope parameter describing the extent of stomatal opening at low light intensities. The wavelength band 400 – 700 nm to which plant chlorophyll responds to is called photosynthetic active radiation (PAR). Its integral is the photosynthetic photon flux density (PPFD).

In the DO₃SE model, Soil Water Potential (SWP) across a PFT specific root depth is simulated according to the Penman–165 Monteith energy balance method that drives water cycling through the soil–plant–atmosphere system (Büker et al., 2012). The stomatal response to changes in SWP (f_{SWP}) are, thus, given by:

$$f_{\text{SWP}} = \min \left\{ 1, \max \left\{ f_{\min}, \frac{(1 - f_{\min}) \cdot (\text{SWP}_{\min} - \text{SWP})}{\text{SWP}_{\min} - \text{SWP}_{\max}} + f_{\min} \right\} \right\} \quad (9)$$

where SWP_{\min} and SWP_{\max} are the parameters describing the f_{SWP} relationship.

2.1.2 Gap filling methodology

170 The DO₃SE model requires hourly, continuous input data. Therefore, the following gap filling methodology was devised for the meteorological drivers of the model:

- Single hours of missing data were filled by taking the average of the hourly values before, and after, the missing value.
- Several consecutive hours of missing data (23 or less) were filled by taking the average of the corresponding hour the day before, and the day after; and repeating this for each missing hour of data. If data were unavailable from that hour of the previous day, then only the value from the day after was used and vice versa. Interpolated values were not used in calculating averages.

- Data gaps longer than 24 h were filled using weekly diurnal averages. i.e. an average was calculated using the corresponding hour throughout the week before and after. Interpolated values were not used in calculating averages.

To fill gaps in the ozone data, we applied the methodology described in Falk et al. (2021) that is based on a Reynolds
180 decomposition of the form:

$$[\text{O}_3] = \langle [\text{O}_3] \rangle + \Delta[\text{O}_3], \quad (10)$$

with an ozone climatology (multiannual norm) $\langle [\text{O}_3] \rangle$ and ozone anomalies (deviation from the norm) $\Delta[\text{O}_3]$. Falk et al.
185 (2021) computed a generalized climatology for northern Fennoscandia from long-term records of different close by sites and determined the station with the highest correlation coefficient compared to the site with the gap. For this site, the anomalies with respect to the generalized climatology were calculated for the gap period. These anomalies were then added to the climatology
190 of the site with the gap and corrected for an increase in present-day tropospheric background ozone compared to the early 1990s. For more details and a comparison with regional air quality models refer to Falk et al. (2021).

2.1.3 Input data and observation site



The required input data consists of ozone concentration $[\text{O}_3]$, 2 m temperature $T_{2\text{m}}$, global irradiation Q_0 , precipitation, 2 m
190 wind $u_{2\text{m}}$, and vapor pressure deficit VPD. VPD has been calculated from observed $T_{2\text{m}}$ and relative humidity

$$\text{VPD} = P_s(T) \cdot \left(1 - \frac{\text{relHum}}{100} \right), \quad (11)$$

with saturation vapor pressure $P_s(T)$ in hPa from the Arden Buck equation (Buck, 1981; Buck Research Instruments, LLC,
2012).



For our study, we chose Svanhovd in northern Norway (69.45°N , 30.03°E , 30 m a.s.l.). Reasons for our choice were: (1)
195 Ambient ozone concentration had been monitored there in the past, (2) an agrometeorological station is measuring, e.g. 2 m
temperature, precipitation, global irradiance, and soil temperature at different depths, and (3) a national surveillance of air
pollution (NO_x , SO_x , particular matter (PM), radiological species) is ongoing. Most of these measurements are performed by
the Norwegian Institute for Air Research (NILU), who also conducted ozone measurements on our behalf during the 2018/19
growing season.

200 All essential climate variables for the 2018/19 growing season were provided by NILU through the web portal luftkvalitet.no
(last accessed May 2020). The ozone monitoring data have been added to a database for air-quality monitoring called EBAS
as well operated by NILU and are thus openly accessible. Long-term ozone observation data (1986–1996) were obtained
from EBAS. Note that data from before the 1990s do not follow the high-quality standard procedures implemented nowadays
and have to be treated with care (Solberg, 2003). Because ozone monitors did not undergo regular re-calibration, shifts in the
205 observed data occurred imposing false trends which are small but in the same order of magnitude as the expected trends in
tropospheric background ozone. This does not concern the ozone seasonality which we are particularly interested in. The long-
term data sets of agrometeorological variables including temperature and precipitation are available from September 1992 to
the present day (LandbruksMeteorologiske Tjeneste NIBIO, note the station name here is Pasvik).



To relate local ozone concentration [O_3] with visible damage on ozone sensitive plants, an ozone bio-monitor (referred to as ozone garden) has been installed at Svanhovd in the 2018/19 GS. The locations of the atmospheric monitoring site and the ozone garden are marked in the aerial photography shown in Fig. 1a. An ozone garden consists of selected plant species that are sensitive to ozone and are likely to display visible injuries. Cultivated species were, e.g. clovers (*Trifolium repens*, *Trifolium pratense*), tobacco (*Nicotiana tabacum*, cultivars Bel-W3, Bel-B and Bel-C), and potato (*Solanum tuberosum*). As shown in Fig. 1b, the plants had to be protected from herbivores with a wire-mesh fence. In 2018, we qualitatively observed visible ozone damage on semi-natural vegetation (clover) and crops (tobacco). In contrast, no such visible damage was found on the clovers in 2019, although it was observed on the sensitive tobacco cultivar (Bel-W3). Note that the extent of visible damage is not equivalent to a quantitative reduction of above/below ground biomass of a species.

2.2 Model parameter localization

We determined the dominant species on-site at Svanhovd from Fig. 1a and found perennial grassland, birch (generalized as deciduous trees), and Scots pine (generalized as coniferous trees). Basic parameters for these PFTs are derived from Simpson et al. (2007); Mills et al. (2011, 2017) and will be referred to as mapping manual (MM) parameterizations. The localization of parameters for coniferous trees is based on MM's Boreal Norway spruce, deciduous trees on MM's silver birch, and perennial grassland on MM's perennial grassland for Central Europe. For a comprehensive list of MM parameters, consult Supplement Table S1. In the following, we suggest localizations of key environmental parameters to a subarctic climate based on meteorological data to assess over-/underestimation of ozone damage when using MM Boreal parameterizations in ozone risk assessments.

2.2.1 Temperature and light response

Initial simulations with the MM parameterizations for perennial grassland revealed an unexpected low stomatal conductance at leaf-level ($G_{\text{sto}}^{\text{leaf}}$) in 2019 (Appendix Fig. B1). Substantial stomatal conductance occurred only during an extended warm period in late July. In ecological terms, this means that there would have been almost no growth of grass in the summer of 2019 – a model prediction that is falsified by reality. We identified f_T as abnormally low throughout the season, being the limiting factor of stomatal conductance in perennial grassland. This suggested that a localization of the parameterization to a subarctic climate was necessary.

To localize the temperature response function f_T , we divided the temperature dataset into two subsets: 1992–2000 (near past) and 2011–2019 (present). From these two subsets, we selected only dates within the GS (May–September) and plotted the probability density functions (PDFs) as histograms with 1 °C binning (Fig. 2a). A comparison between the two PDFs indicates that the temperature distribution has shifted towards higher temperatures reducing the number of days below 5 °C. It is unclear how fast the species composition of perennial grassland responds to these changes. Thus, the predominant acclimation at present is not known. Further, we overlaid these histograms with the MM f_T . A low overlapping area suggests a low agreement with local climate conditions.

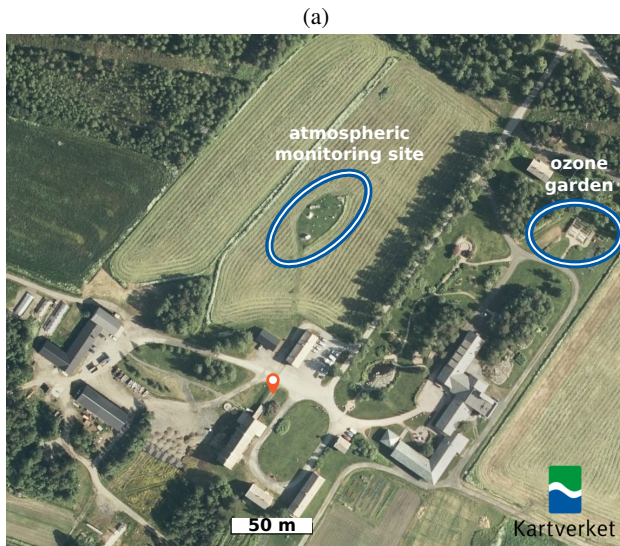


Figure 1. NIBIO Environment Centre Svanhovd close by the settlement of Svanvik, Norway. (a) Atmospheric monitoring site and ozone garden have been marked. Aerial photography ©Norges Kartverk; (b) Clovers in the Svanhovd ozone garden. The plants had to be secured against herbivores with a wire-mesh fence. The plants shown are approximately 6 – 12 cm high.



Hence, the idea was to define localized temperature response functions by increasing the overlapping area between f_T and the temperature PDF during the GS. To this end, we defined two different hypothetical target species: *subarctic* and *cold*. We constructed *cold* as representative for a species that is more tolerant to cold temperatures than *MM*, but slightly less efficient at warm temperatures than *MM*. This was accomplished by moving T_{\min} and T_{opt} towards cooler temperatures but T_{\max} was kept at its *MM* value. In the same way, *subarctic* was constructed to represent a species that is very tolerant to cold but sensitive to high temperatures, and most efficient at cool temperatures. Therefore, we shifted both T_{\min} and T_{\max} to

245



colder temperatures and chose T_{opt} close to the climatological mean temperature of 1992–2000. The most extreme of the two localizations compared to MM is *subarctic*.

For localizing f_{light} , we presumed that the opening extent of stomata at low light conditions differs in subarctic species compared to species in less extreme climates. We, therefore, adjusted the modelled light sensitivity of stomata such that the PPFD value needed to reach 50 % opening is varied by $\pm 20 \%$. For this, we derive the inverse function $f_{\text{light},k}^{-1}$ of Eq. (8) for each PFT k analytically

$$\gamma_k(f_{\text{light}}) := f_{\text{light},k}^{-1} = -\frac{\ln(1-f_{\text{light}})}{\alpha_k}. \quad (12)$$

First, we solved Eq. (12) for the MM default value of α_{MM}^k at 0.5 (50 % opening)

$$255 \quad \gamma^k(0.5) = -\frac{\ln(0.5)}{\alpha_{\text{MM}}^k}, \quad (13)$$

and defined a variation $\gamma' = \gamma \cdot \eta$ with $\eta \in \{0.8, 1.2\}$. By solving Eq. (12) for α , we find $\alpha'(\gamma')$.

In Fig. 2b, we show the PPFD PDF for near past and present together with the f_{light} for perennial grassland. The MM parameterization is displayed as solid line.

Similarly, we defined localized f_T and f_{light} for coniferous and deciduous trees. The resulting response functions are shown in Appendix Figs. B3 and B4, respectively. Coniferous trees are known to start photosynthesis as soon as the leaf temperature reaches a certain threshold (Kolari et al., 2007). Thus, coniferous trees are already active at low air temperatures and can reach 60 % photosynthetic activity as early as doy 100 but cease activity in less favorable conditions (Kolari et al., 2007; Wallin et al., 2013). To determine the temperature localization for coniferous trees, we used the time series of CO₂ uptake and temperature at observation sites in southern (\rightarrow cold) and northern (\rightarrow subarctic) Finland by Kolari et al. (2007). From these, we estimated an optimal temperature interval ($10^\circ\text{C} \leq T_{\text{opt}} \leq 15^\circ\text{C}$). For simplicity, the same interval was assumed for deciduous trees.

All resulting temperature response function localizations are tabulated in Table 1 and light response function in Table 2. In Section 3.1, we compare relative g_{sto} based on Eq. (5) for the different localizations using the long term meteorological data.

2.2.2 Growing season estimate

The accumulation of ozone dose is strongly depended on the timing and length of the GS. Mills et al. (2017) suggest a simple latitude model for beech, birch, and Norway spruce for the localization of GS:

$$A_{\text{start}} = 105 + (\text{LAT} - 50^\circ\text{N}) \cdot 1.5 \quad (14)$$

$$A_{\text{end}} = 297 - (\text{LAT} - 50^\circ\text{N}) \cdot 2 \quad (15)$$

At Svanhovd, this yields $A_{\text{start}} = 135 \text{ doy}$ and $A_{\text{end}} = 257 \text{ doy}$. We verified these as follows.

For coniferous trees, we used a MODIS (Aqua/Terra) retrieved GPP product (Running et al., 2015) on a $1 \times 1 \text{ km}$ patch centered at Svanhovd. GPP over time follows approximately a second-order polynomial function (Fig. B2). By calculating the roots of the fitted polynomial, we found A_{start} as doy 122 for 2018 and doy 106 in 2019. A_{end} amounts to doy 261 and 274,

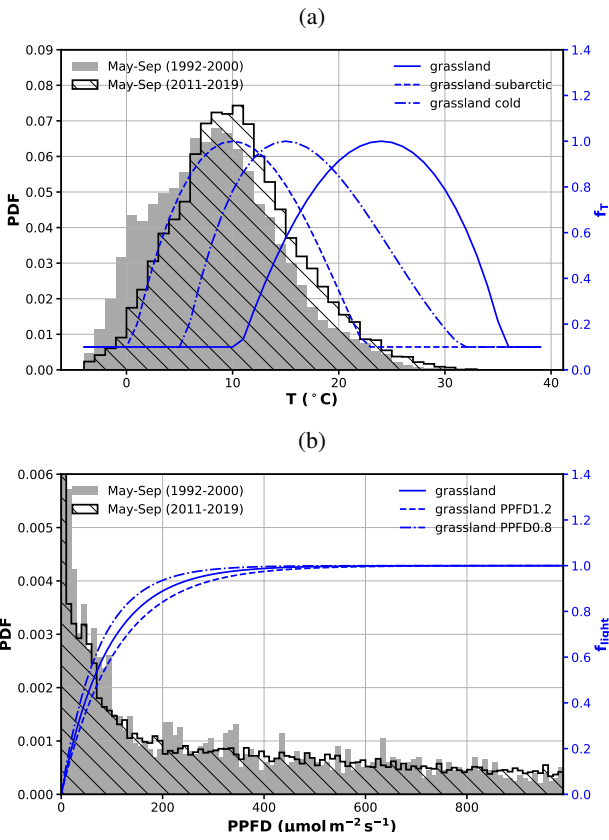


Figure 2. Construction of bespoke response functions for grassland. (a) f_T and (b) f_{light} are shown together with underlying T_{air} and Q_0 climatologies (probability density function - PDF), respectively. Original mapping manual parameterization is shown in comparison as solid line. Note that Q_0 has been truncated to 0.006. PPFD0.8 and PPFD1.2 refer to α values increasing/decreasing PPFD at $f_{\text{light}} = 0.5$ by $\pm 20\%$, respectively.

respectively. This A_{end} value will be used for all PFTs alike. The resulting growing season for coniferous trees in 2019 was one month longer than in 2018. For A_{start} of deciduous trees, we use temperature-degree-days (above 5°C) on gridded temperature data from SeNorge.no (Appendix Fig. A1). We found doy 129 and 130, respectively. For both years, these dates coincide with 280 the first snow-free day at the closest inland meteorological weather station at Øvre Neiden (Sør-Varanger, NOR) and are very similar to the latitude model predictions. For perennial grassland, we assume a latency period of 1 month after snow-melt. This assumption is supported by observations in Rovaniemi, Finland (Korhonen et al., 2018, Supplement Fig. S1). All results are tabulated in Table 3.

2.2.3 Other properties

285 Soil texture influences water availability and thus POD_y calculations in DO₃SE (Büker et al., 2012). The soil at Svanhovd is characterized in an ICP Forest plot survey as gleyic cambisols according to the Food and Agriculture Organization of the

Table 1. Bespoke temperature parameterizations. MM refers to mapping manual (Mills et al., 2011, 2017).

Species	type	T_{\min}	T_{opt}	T_{\max}
Deciduous tree	MM	5	20	100
	Cold	5	15	100
	Subarctic	0	10	100
Coniferous tree	MM	0	20	100
	Cold	0	15	100
	Subarctic	0	10	100
Perennial grassland	MM	10	24	36
	Cold	5	15	36
	Subarctic	0	10	24

Table 2. Bespoke light parameterizations. MM refers to mapping manual (Mills et al., 2011, 2017).

Species	type	α	$\gamma(0.5)$
Deciduous tree	MM	0.004	165.035
	PPFD0.8	0.005	132.028
	PPFD1.2	0.003	198.042
Coniferous tree	MM	0.006	115.525
	PPFD0.8	0.008	92.420
	PPFD1.2	0.005	138.629
Perennial grassland	MM	0.011	63.013
	PPFD0.8	0.014	50.411
	PPFD1.2	0.009	75.616

United Nations (FAO) soil classification system and as eluviated dystric brunisol in the ICP Forest soil classification system (V. Timmerman, personal communication, June 2020). The clay:sand:silt content is estimated to range from 12 %:61 %:27 % at the top layer to 16 %:59 %:25 % in about 1 m depth (soilgrids.org, last accessed April 2022 for location 30.0334°E, 69.4549°N)

290 Within the DO₃SE soil parameterization, the sandy loam texture describes the upper 60 cm, where the plant roots are found, of this soil type best. 

We did not perform a focalization of the water vapor pressure deficit f_{VPD} and soil water potential f_{SWP} response functions. But acknowledge that these are very important factors in the modeling of ozone dose as pointed out by Büker et al. (2012).

The quasi-laminar boundary layer resistance R_b is a function of wind speed u and influenced by the tree height and leaf dimensions. For comparison with MM, we collected a sample of birch (*B. pubescens*) leaves from the outer canopy (good

Table 3. Start and end of growing season in doy. Central Europe is shown for comparison.

Species	Year	A_{start}	A_{end}
Central Europe ^b	–	100	307
Latitude model (70°N) ^b	–	135	257
	2018	129 [*]	261 ^a
Deciduous tree	2019	130 ^c	274 ^a
	2100	116 ^e	286 ^e
Coniferous tree	2018	122 ^a	261 ^a
	2019	106 ^a	274 ^a
Perennial grassland	2018	159 ^d	261 ^a
	2019	161 ^d	274 ^a

^a MODIS (Aqua/Terra) GPP product;

^b Mills et al. (2017),

^c 5 days – 5°C -rule, T_{air} from seNorge.no;

^d One month after snowmelt; reference station Øvre Neiden (Sør-Varanger, NOR)

^e Future projection based on linear regression of ^c (Fig. A)

light exposure) of tall trees at two sites in Finnmark. The leaves were collected late in July, thus, they were fully expanded. They were collected by hand at about 2 m height. As the sun is at a low elevation angle for most of the time in the growing season in this area, light exposure at the top of the tree is not expected to be different from lower leaves as long as they grow in a part of the tree that is not shadowed by other trees. At the first site (Karasjok), three leaves were collected from five adult trees each.

300 At the second site (Svanvik), five leaves were collected from one tree. The leaves were pressed and dried before scanning for the area and shape determination through image analysis. ImageJ (see webpage) was used for thresholding the images to give silhouettes of the leaves. After scaling the images, the program was used to find the minimum Feret diameter. This measure finds the largest width of a leaf at a 90° angle to the length of the leaf (the Feret diameter). With this method we found that the 20 leaves had a mean width of (3.0 ± 0.5) cm that is smaller than in the MM parameterization (5 cm, Supplement Table S1).

310 A report by Systad et al. (2004, p. 52) indicated an average tree height of 13.5 m in the Svanhovd area. One Scots pine forest at Svanhovd has been studied as a part of the ICP Forest mapping. There, heights were measured in 2004 when the stand was 90 years old. The mean tree height was 10.1 m and maximum height was 16.2 m (V. Timmerman, personal communication, June 2020). We used 13.5 m for both deciduous and coniferous trees as this height is found from a larger and more diverse population of species.

3 Results

In this section, we first compare the average stomatal conductance $\langle g_{\text{sto}} \rangle$ relative to g_{ref} for each PFT from the long term meteorological data according to Eq. (5) and compare the different localizations to MM (Section 3.1). We use the DO₃SE

model to compare the ozone dose and projected biomass loss due to ozone for the two cent GSs 2018/19 for each species and localization (Section 3.2). Finally, we put the results into a climatological perspective (Section 3.3.2).

315 3.1 Parameter localization

We presume that perennial vegetation will likely maximize carbon acquisition during the short subarctic growing season. Because the MM version of the DO₃SE model currently does not simulate net photosynthesis A_n , we assume a first order proportionality between A_n and g_{sto} (Medlyn et al., 2011). A higher average $\langle g_{\text{sto}} \rangle / g_{\max}$ ratio, thus, indicates a higher growth potential in the local climate.

320 We propose the following metric. From the long term of meteorological data, we select two distinct periods: noon (11 am – 1 pm local time) and morning (5–9 am local time) and calculate the average relative stomatal conductance $\langle g_{\text{sto}} \rangle / g_{\max}$ (Eq. (5) assuming $f_{\text{SWP}} = 1$). Presumably, $\langle g_{\text{sto}} \rangle / g_{\max}$ around noon (the highest light intensity) is a good proxy for CO₂ uptake efficiency (growth). In addition, a small deviation between noon and morning and a low standard deviation indicates higher robustness of this localization to variability in growth conditions. From left to right in Fig. 3, results using the subarctic, cold, 325 and MM are shown marked by an alternating background color. Within each of these groups f_{light} categories are indicated by PPFD0.8 and PPFD1.2, respectively. The standard deviation is denoted with error bars.

Based on the above criteria, we identify *subarctic*–PPFD0.8 as the parameterization with the highest score. The differences between the localized parameterizations and the MM are smallest for coniferous trees. This indicates that the MM Boreal parameterization is well suited for the subarctic climate at Svanhovd. For perennial grassland, the differences compared to 330 MM are largest suggesting that the *Central European* parameterization is not appropriate in a subarctic climate. Deciduous trees display also a notable increase in mean stomatal conductance using our localizations.

3.2 Implications on ozone risk assessments

We modeled POD_y with a flux threshold $y = 1 \text{ nmol m}^{-2} \text{ s}^{-1}$ per PLA for the three natural/semi-natural vegetation types, 335 deciduous trees, coniferous trees, and perennial grassland using the MM parameterization and our localized temperature (*cold*, *subarctic*) and light (PPFD0.8, PPFD1.2) parameterizations.

The results are comprehensively displayed in Fig. 4. Critical levels for reduction in biomass (deciduous forest 4 %, coniferous forest 2 %, and grasslands 10 % biomass reduction adopted from Mills et al., 2017; Hayes et al., 2021) are shown as horizontal dashed lines. The different background colors indicate the temperature response function localization. The light response function localizations are denoted + (PPFD1.2) and – (PPFD0.8). Circles indicate simulations with localized GS, canopy height, and leaf dimensions, TODO: (whereas squares indicate simulations with MM GS for Central Europe. We compare this to demonstrate the impact of a projected prolonged GS in the future.) With open symbols, the effect on POD_y with SWP taken into account is displayed.

We identified in general that an increasing cold tolerance represented by a in the temperature response function (MM < cold < subarctic) leads to an increase in POD₁ in both probed years. TODO: (while using locally adapted GS causes a 345 reduction.) An earlier start and overall longer GS in 2019 leads to higher POD₁ compared to 2018 despite the occurrence

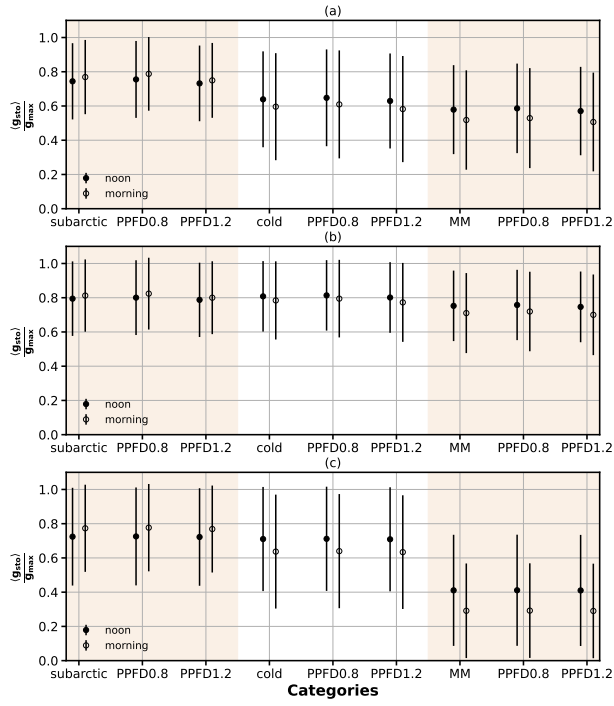


Figure 3. Proposed metric to test bespoke response functions. GS (May–August) climatological averages and standard deviation of g_{sto}^k (Eq. (5)) relative to g_{max}^k at noon (averaged over 11 am – 1 pm local time) and in the morning (averaged over 5 – 9 am local time) are shown for (a) deciduous trees; (b) coniferous trees; (c) perennial grassland.

of more episodes of elevated O₃ in 2018 than in 2019 (see Section 3.3.3 for details). Taking into account SWP, POD₁ was effectively only reduced for deciduous trees in 2018, while in all other cases simulation results with and without SWP effects were identical. An earlier opening of stomata at low light intensities (PPFD0.8) caused an increase in POD₁ compared to MM while a later opening (PPFD1.2) reduced POD₁. Due to the shape of f_{light} , a symmetric variation can lead to an asymmetric response in POD₁.

For deciduous trees (Fig. 4a) all POD₁ simulations exceed the CL by TODO: (5 – 25 mmol O₃ m⁻²) and display the largest spread in POD₁ with respect to f_{light} . In 2019, the lowest estimated POD₁ (MM, PPFD1.2) amounts to 10 mmol O₃ m⁻², while the highest estimate (subarctic, PPFDO.8) reaches about 20 mmol O₃ m⁻². In 2018, the uncertainty range is much smaller ((12–18) mmol O₃ m⁻²). In particular, the impact of f_{light} is pronounced (extent of $\angle(+, 0, -)$). The maximum difference in POD₁ due to the f_{light} localization for the PPFDO.8 (superscript) and PPFD1.2 (subscript) amount to $^{+1.6}_{-2.3}$ mmol O₃ m⁻² for 2018 and $^{+1.9}_{-2.7}$ mmol O₃ m⁻² for 2019. The difference in POD₁ compared to MM in response to the localization of f_T and GS ranges between $\Delta \text{POD}_1 = (1.4 – 3.6)$ mmol O₃ m⁻² in 2018 and $\Delta \text{POD}_1 = (2.7 – 7.7)$ mmol O₃ m⁻² in 2019. A low soil water potential caused a reduction in POD₁ in 2018 in cases when using PPFDO.8. This indicates that drought conditions



can reduce the ozone damage risk. TODO: (With MM GS, POD₁ values were higher in 2018 than in 2019. However, taking 360 the localized GS into account, this is reversed for the subarctic temperature response function. This can be explained by more favorable growing conditions in 2019.)

For coniferous trees (Fig. 4b), most simulations slightly exceed the CL ($0 - 10 \text{ mmol O}_3 \text{ m}^{-2}$). Our localization does not show much difference compared to MM indicating the the MM Boreal Norway spruce parameterization was already well-adjusted to the local subarctic climate. We find a higher POD₁ in 2019 than in 2018. The maximum difference in 365 POD₁ determined between localized GS for subarctic and cold parameterizations with respect to MM ranges between ($0.5 - 1.0 \text{ mmol O}_3 \text{ m}^{-2}$ in 2018 and $(2.0 - 3.3) \text{ mmol O}_3 \text{ m}^{-2}$ in 2019). The maximum difference determined from PPFD0.8 (superscript) and PPFD1.2 (subscript) f_{light} amounts to $^{+1.0}_{-0.8} \text{ mmol O}_3 \text{ m}^{-2}$ for 2018 and $^{+1.3}_{-1.0} \text{ mmol O}_3 \text{ m}^{-2}$ for 2019.

For perennial grassland (Fig. 4c), all simulations with localized GS stay below the CL. Perennial grassland shows the smallest POD₁, but a similarly large response to the temperature parameterization localizations as deciduous trees. Again, we find a 370 reversal for predicted ozone risk in 2018 and 2019 for the subarctic type. Perennial grassland shows the lowest sensitivity to the light threshold. TODO: (and SWP is only relevant without localized GS (see above).) The overall difference in POD₁ determined from the localized GS for subarctic and cold types with respect to MM ranges between ($2.2 - 3.4) \text{ mmol O}_3 \text{ m}^{-2}$ in 2018 and $(4.4 - 6.4) \text{ mmol O}_3 \text{ m}^{-2}$ in 2019. The chosen lower maximum temperature in the subarctic parameterization probably caused the lower POD₁ in 2018 (warm year) compared to the cold parameterization. This was not seen in 2019. The 375 maximum difference in POD₁ determined from the PPFD0.8 (superscript) and PPFD1.2 (subscript) variation of f_{light} amount to $^{+0.3}_{-0.2} \text{ mmol O}_3 \text{ m}^{-2}$ and $^{+0.3}_{-0.3} \text{ mmol O}_3 \text{ m}^{-2}$, respectively.

The maximum difference in POD₁ between simulations with the MM parameterizations and localized temperature and light response functions is of the same order of magnitude as the difference between the two probed years. The magnitude of 380 all described effects on POD₁ varies between PFTs as well as years, but is by construction always larger than estimated with the MM parameterization. This means that the ozone damage risk could be possibly underestimated even in normal years and establishing dedicated subarctic parameterizations are a must to properly assess ozone damage risk in these regions.

We estimated the biomass reductions in accordance to the CLs (Mills et al., 2017; Hines et al., 2021) for the most extreme temperature parameterization localization (*subarctic*) for each PFT. The estimates for SWP=off are listed in Table 4. We defined an uncertainty range from the difference in biomass reduction caused by the variation of f_{light} . superscript refers to 385 PPFD0.8 and subscript to PPFD1.2. The reported range corresponds to the effect of taking SWP into account or not. As SWP reduces POD₁, biomass reduction is decreased when taking SWP into account. The biomass reduction ranges between 2.5% (coniferous, 2018) and 17.4% (deciduous, 2019). For deciduous trees this amounts to a reduction by up to 55% compared to MM. Coniferous trees are the least affected PFT and the magnitude of total biomass reduction is almost independent of the choice of the parameterization within given uncertainties.

390 3.3 Climate and weather conditions in the growing season 2018/19

Here, we put weather conditions during the growing season 2018/19 into a climatological context. All relevant data for the 395 growing season 2018/19 are shown as time series in Fig. 5. Ozone concentrations measured at 2m height above ground are



Table 4. Estimated total biomass reduction in % for temperature acclimation *subarctic* with localized GS and SWP=off. The uncertainty ranges reported here correspond to maximum a divergence deducted from varying f_{light} and SWP=on. For comparison, the corresponding biomass reduction for the MM parameterization averaged over both years is shown. In this case, standard deviation is computed from all sensitivity simulations ($\pm 20\%$ in extent of stomatal opening at low light, SWP on/off, and localized GS).

Year	PFT			
	Deciduous tree	Coniferous tree	Perennial grassland	
			total	above ground
2018	15.5 ^{+(1.9...2.1)} _{-(0.8...1.5)}	2.5 ^{+0.2} _{-0.2}	9.7 ^{+0.2} _{-0.2}	12.4 ^{+0.2} _{-0.2}
2019	17.4 ^{+2.5} _{-1.8}	3.0 ^{+0.2} _{-0.3}	10.5 ^{+(0.1...0.2)} _(0.0...0.1)	13.7 ^{+(0.1...0.3)} _(0.1...0.3)
$\langle \text{MM} \rangle$	11.2 \pm 1.1	2.31 \pm 0.04	7.5 \pm 0.9	9.6 \pm 1.4

averaged hourly. The hatched areas mark times when no ozone data were recorded. Note, while the downtime during winter was planned, missing data in two weeks of July 2018 (July 9–23) were due to problems in data acquisition.

395 3.3.1 Weather conditions

As can be seen in Fig. 5a, χ_{O_3} peaks in spring (April/May) and reaches its minimum in late summer (July/August). The spring peak has not been captured completely in 2019, since data acquisition only started in late April. In summer 2018 (June–August), high ozone concentrations ($\chi_{\text{O}_3} > 40 \text{ ppb}$) were recorded 50 times. The highest summer ozone VMR ($\chi_{\text{O}_3} = 50.2 \text{ ppb}$) was measured on July 25. This coincides with the period of the most extensive forest fires in central Sweden which occurred from 400 July 12–29 (Björklund et al., 2019). However, due to the above-mentioned data acquisition problems, we missed most of the corresponding ozone data for this event and most likely also the peak χ_{O_3} . A method for gap-filling these data has been presented in Falk et al. (2021) and explained in Section 2.1.2. In contrast, χ_{O_3} only rose 18 times above the threshold of 40 ppb during the summer of 2019.

Hourly averaged 2 m temperatures above 20 °C occurred more regularly in July 2018 than in 2019 (Fig. 5b). In 2018, spring temperature regularly rose above freezing only in May, while in 2019 this occurred already early in March/April indicating a later start of the GS in 2018. More rain events with accumulated daily precipitation ($\sum_d \text{Precip}$) above 10 mm occurred in the summer of 2018 compared to 2019 (Fig. 5c). Qualitatively, global irradiance (Q_0) displayed in Fig. 5d was higher in May and July 2018 compared to 2019, while June 2019 showed higher irradiance than in 2018. A high global irradiance, in most cases, is the result of a low cloud fraction. In both years, the maximum recorded Q_0 was 750 W m^{-2} and reached in June.

410 3.3.2 Climate (1990-present)

Climatologies (typically multi-year monthly averages) of temperature, precipitation, and radiant energy Q_e for Svanhovd were derived for the period 1992–2012 and are shown as box plots in Fig. 6. Therein, the colored horizontal lines indicate the median and the triangles the mean value for the respective month. A box denotes the interquartile range (IQR). Observations exceeding

1.5 times the IQR (whiskers) are usually considered outliers but ought to be interpreted differently in a climate diagram, namely

415 as events deviating extraordinarily from the norm.

Temperatures usually stay below freezing for 5 consecutive months, while only 2 months breach 10°C regularly (July, August), satisfying the conditions for a Köppen's climate classification of a regular subarctic climate (Dfc) (e.g. Beck et al., 2018). The highest monthly average temperature is $(13.1 \pm 1.1)^{\circ}\text{C}$ in July and the lowest $(-12.8 \pm 2.0)^{\circ}\text{C}$ in February. The coldest ever recorded temperature was -45.2°C on January 27, 1999, while the highest temperature (29.4°C) occurred on

420 July 16 the same year. As can be seen mean and median are well aligned in the center of the IQR for most months meaning that temperature anomalies are symmetrically distributed.

The average accumulated monthly precipitation ($\sum_d \text{Precip}$) indicates that winter and spring (November–April, except for March) are relatively dry ($\sum_d \text{Precip} < 20 \text{ mm}$). March precipitation is primarily snow and will influence the start of the growing season. The driest month is January with $\sum_d \text{Precip} = (16.7 \pm 3.0) \text{ mm}$. The most precipitation occurs in summer, with

425 a $\sum_d \text{Precip} = (58.5 \pm 9.2) \text{ mm}$ in August. The average annual accumulated precipitation ($\sum_m \text{Precip}$) given with standard error of mean is $(383 \pm 86) \text{ mm}$. Mean and median precipitation are less well aligned compared to temperature and point to a considerable interannual variability.

The climatology for global radiant energy Q_e in J m^{-2} (the integral of Q_0) is zero in November–January (polar night) and reaches its maximum in May–July (midnight sun conditions). Mean and median are well aligned. Only June displays a slightly

430 skewed distribution towards higher Q_e .

The ozone VMR climatology (χ_{O_3}) (1986–1996) is shown in Figure 6d. The climatological spring peak occurs in April (around doy 100) and amounts to 40 ppb while the annual average χ_{O_3} was 28 ppb. The decline in χ_{O_3} roughly coincides with the beginning of CO₂ uptake by coniferous trees (Kolari et al., 2007; Wallin et al., 2013). Mean and median are well aligned and centered indicating a symmetric distribution for each month. The highest recorded χ_{O_3} occur in June most likely due to

435 forest fires as mentioned above.

3.3.3 2018/19 growing season anomalies

In climate science, a tool to compare specific years anomalies – the deviation from the norm – are used. In Figure 7, we show anomalies for both temperature, precipitation, radiant energy, and ozone VMR. We defined anomalies as median deviation from the climatological median. The hatched area indicates the respective IQR.

440 Temperature anomalies (Fig. 7a) show enhanced temperatures throughout summer (May–September) 2018 breaching the IQR two times while March was unusually cold. No notably enhanced temperatures occurred in 2019 indicating that 2019 was an average year.

Similarly, the precipitation anomalies are displayed in Fig. 7b. March 2018 saw more precipitation than usual but mainly as snow. May and October were unusually dry while August was unusually wet. 2019 was rather average throughout the year, but

445 unusually wet in June and dry in July.

Radiant energy anomalies are presented in Fig. 7c. In summer 2018 (May/July), Q_e was extraordinarily higher than usual, while 2019 was generally an average year with a rather dark spring (April/May) and late summer (August).

We used the bias-corrected and cross-calibrated ozone climatology (Falk et al., 2021) to assess the ozone anomalies in 2018/19. Note that we have not recorded ozone during winter (refer to Section 3.3.1). In April/May 2018, ozone was unusually 450 elevated and stayed higher than usual through the whole GS. The highest anomaly in 2019 occurred in September at the end of the GS. The forest fires in Sweden in July enhanced ozone notably at Svanhovd.

4 Discussion and conclusions

We found that 2018 was warmer, slightly drier, and brighter than usual, while 2019 was a rather average year at Svanhovd. According to a report by the Norwegian Meteorological institute (Gangstø Skaland et al., 2019), the summer of 2018 was 455 the warmest and driest ever recorded in eastern, western, and southern Norway. In the north (including Finnmark), it was amongst the warmest on record. Thermal stress on vegetation was exceptional not only in large parts of Fennoscandia but also in much of Europe, where the influence of the blocking high-pressure system extended even over five months (April/May, July–September). These conditions gave rise to massive forest fires in different parts of Europe. A total of 2079 forest fires were registered in Norway in 2018, twice as many as in the preceding years 2016/17 (DSB, 2019, last accessed April 2020). In 460 Sweden, about 500 fires had been reported (five times more than in a usual summer), and an estimated total of 25000 hectare burned down in central Sweden (Björklund et al., 2019). We found coincident peak χ_{O_3} in ozone monitoring data at Svanhovd in July. Overall, ozone was more enhanced in 2018 than 2019. It is very likely that elevated ozone, like during the 2003 drought period (Solberg et al., 2008), was promoted by a combination of various factors such as wildfires, reduced cloud cover (increased solar radiation), reduced dry deposition and turbulent mixing due to the stagnant weather conditions, and increased 465 BVOC emissions. As such events may become more frequent in the future, conditions at Svanhovd for the growing seasons 2018 could serve as a reference for probable future conditions in northern Fennoscandia and arising ozone-induced damage risk. Conditions in 2019 represent the present climate.



Taking a presumed adaption of vegetation to local climate into consideration, we derived localized Jarvis-type temperature and light response functions for modeling POD_1 and biomass reduction with the DO_3SE model. Our key findings are that 470 vegetation that is more sensitive to warm temperatures would be less effected by coincident ozone and heat stress because stomata will close to prevent water loss whereas vegetation adapted to warmer climate zones could be under higher ozone damage risk under these conditions. On the other hand, a warmer climate and hence prolonged GS would negatively affect 475 any vegetation using the POD_y metric. It is essential for ozone risk assessments in the subarctic to define plant physiology and traits such as phenological states properly. As no independent ozone flux measurements are available at Svanhovd, we could not fully validate our methodology at this point. A comparison of DO_3SE model derived dry deposition velocities V_d 480 for coniferous trees with comprehensive records over Pinaceae forests from Hyttilä, Finland (Keronen et al., 2003) (refer to supplementary material Figs. S1–S3) indicate a slightly too high V_d in spring for our most extreme localization (subarctic). No comparable data is available for northern Fennoscandia or deciduous trees and perennial grassland. Perennial grassland and deciduous trees displayed strong susceptibility to our localization methodology (increase in frequency of maximum V_d throughout the GS, see supplementary material Figs. S1–S3) but are within the range ($v_d = (2 – 9) \text{ mm s}^{-1}$ for grassland)

given in the literature (e.g. Jacobs et al., 1992; Padro, 1996; Clifton et al., 2020). Independent flux measurements over these vegetation types in a subarctic climate are thus crucial for evaluation and validation.

Along the conventional ozone monitoring at Svanhovd, we had installed a bio-monitoring with ozone sensitive species. Qualitatively, this showed visible ozone damage  clover and tobacco in 2018. In contrast, no such damage was found on 485 the clovers in 2019. This might indicate a higher ozone damage risk under warmer climate conditions for these specific plant species in a subarctic climate. However, visible damage is not always correlated with a reduction in biomass (Felzer et al., 2007, and citations therein). Also, our DO₃SE modeling results are in contrast to these observations at Svanhovd. Any visible 490 damage caused by peak ozone flux through stomata or a specific dependency of plant sensibility to ozone  phenology stage are not accounted for in the DO₃SE model. In this regard, open-top chamber (OTC) experiments performed in northern Finland where Scots pine and downy birch seedlings were exposed to elevated ozone concentrations attributed a reduction in biomass 495 and reproduction with visible damage explicitly to peak O₃ concentrations and fast phenological development at high growth rate (Manninen et al., 2009). Forbs and perennial grassland are more susceptible to ozone-induced damage in the reproductive state (Bassin et al., 2004). That might explain why we observed damage in the ozone garden to a larger extent in 2019  than in 2018. An associated damage function to ozone depending on leaf age as proposed by Musselman et al. (2006) or phenological 500 state might improve the predictions.

Based on the MODIS GPP product (Running et al., 2015), we estimated the growing season for coniferous trees in 2018 to be at least one month shorter than in 2019. The determined start of growing season in 2018 (doy 122) and 2019 (doy 106) lies within the range given by observations in Fennoscandia (Kolari et al., 2007; Karlsson et al., 2018). We determined the start 500 of the growing season for deciduous trees using growing-degree-days above 5 °C on gridded observational temperature. The results coincide with the first snow free days in our target region. For the period 1994 – 2003 Shutova et al. (2006) reported an observed average start of the GS for mountain birch at Svanhovd at doy 154 and end of GS at doy 229. These dates are well in line with our estimated average start and end of GS for the period 1960 – 2020 (Fig. A1). Our estimates for perennial grassland, are supported by observational data from Rovaniemi (Finland) (Korhonen et al., 2018). The end of GS inferred from the zero-crossing of MODIS observed GPP is in line with independent estimates from the gridded observational temperature. 505 Our method differs from NDVI based determination of GS (Høgda et al., 2001; Karlsen et al., 2007; Høgda et al., 2013). The Shutova et al. (2006) data indicate an earlier end of GS for birch compared to 2018/19. Therefore, POD₁ for deciduous trees could be underestimated by 1.8 mmol O₃ m⁻² in 2018 and 3.0 mmol O₃ m⁻² in 2019, respectively if a climatological GS is used. For perennial grassland the resulting underestimation would amount to 2.0 mmol O₃ m⁻² in 2018 and 2.3 mmol O₃ m⁻² in 2019. This demonstrates the importance of an accurate determination of GS for POD₁ based risk assessments.

510 As shown by Büker et al. (2012), soil water potential is a very important factor for modeling stomatal conductance in the DO₃SE model. Using our best estimate of the soil type at Svanhovd, we found that SWP under 2018/19 meteorological conditions was mainly negligible when considering the localized growing season. We have not assessed the effect of the plants' response to VPD in detail, but the climatological data indicated that conditions at Svanhovd are shifting towards a more VPD limited regime that could limit POD_y under drought stress.

515 Due to a climate change-induced convergence of start of GS with the ozone spring peak (Karlsson et al., 2007), vegetation
might become more exposed to higher ozone concentrations in early phenological stages. However, the decline of this ozone
spring peak is partly caused by dry deposition of ozone to vegetation itself. It, therefore, remains unclear whether an earlier
start of the growing season will increase the exposure of vegetation to ozone or lead to compensation due to an earlier decline
of the peak ozone in the future. Hayes et al. (2021) pointed out that the highest susceptibility of vegetation to future ozone
520 variability is likely to occur in summer when vegetation is most productive. The actual resilience of northern Fennoscandia
plant communities to climate change strongly depends on both the range of acclimation and the type of acclimation. This
means, vegetation that is acclimated to cold temperatures and less to heat- and drought stress might suffer more strongly from
a more frequent occurrence of heatwaves than plants that have a higher temperature tolerance, but our results point to the
opposite concerning the ozone stress.

525 We found that the difference in biomass reduction compared to Boreal parameterizations (Mills et al., 2017) could amount
to 55 % in deciduous trees and 29 – 43 % in perennial grassland. But the biomass reduction functions were established based
on studies from less extreme climates, hence, these results ought to be treated with care. In particular, CLs for deciduous and
coniferous trees were breached in both years and for all parameterizations. For perennial grassland, the CL was not breached
530 if a localized GS was assumed, but the defined CL of 10% loss in biomass might not be transferable to subarctic regions with
considerable constraints on productivity leading to more severe economic consequences.

Beyond the risk assessment of ozone-induced damage, our localized Jarvis-type temperature response functions, once verified by observations, can have important implications on land-surface modeling still using such parameterizations in global models. Problems in productivity of species especially in the Arctic regions occur due to PFTs which are not suitable for the climate. A verification of our proposed methodology by independent flux and dry deposition measurements over birch forest
535 and perennial grassland would be necessary to establish a climate data based localization of stomatal conductance parameterizations.

Data availability. All data is available from public databases or through institutional access. DO₃SE modeling results can be made available upon request.

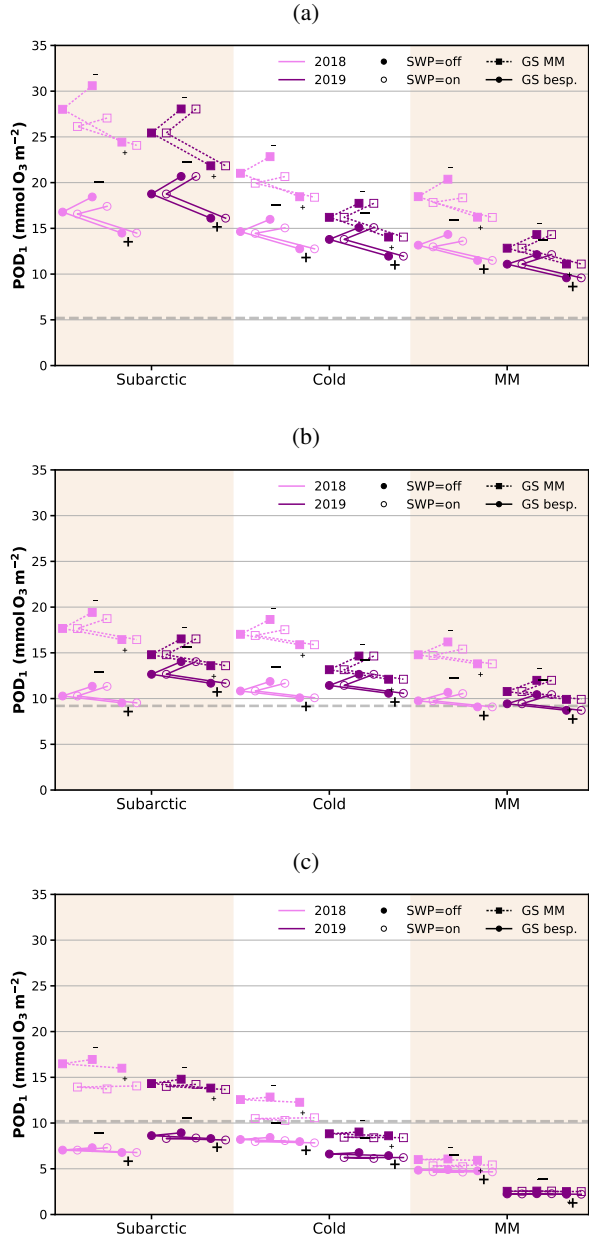


Figure 4. DO₃SE modeling POD₁ results for (a) deciduous trees, (b) coniferous trees, and (c) perennial grasslands at Svanhovd in 2018 (pink) and 2019 (purple). The results varied depending on parameterizations of temperature response functions (MM, Cold, and Subarctic, details in Table 1), growing season (GS MM (squares) or GS bespoke (circles), details in Table 3), light response functions (first, second and third point attached by a line are depicting the MM, PPFD_{0.8} and PPFD_{1.2}, details in Table 2), and the effect of taking SWP into account (filled symbols without and open symbols with effects of drought kept in the model). Critical levels for ozone damage (Mills et al., 2017; Hayes et al., 2021) are given as dashed horizontal lines. Note that the horizontal axis is only categorical.

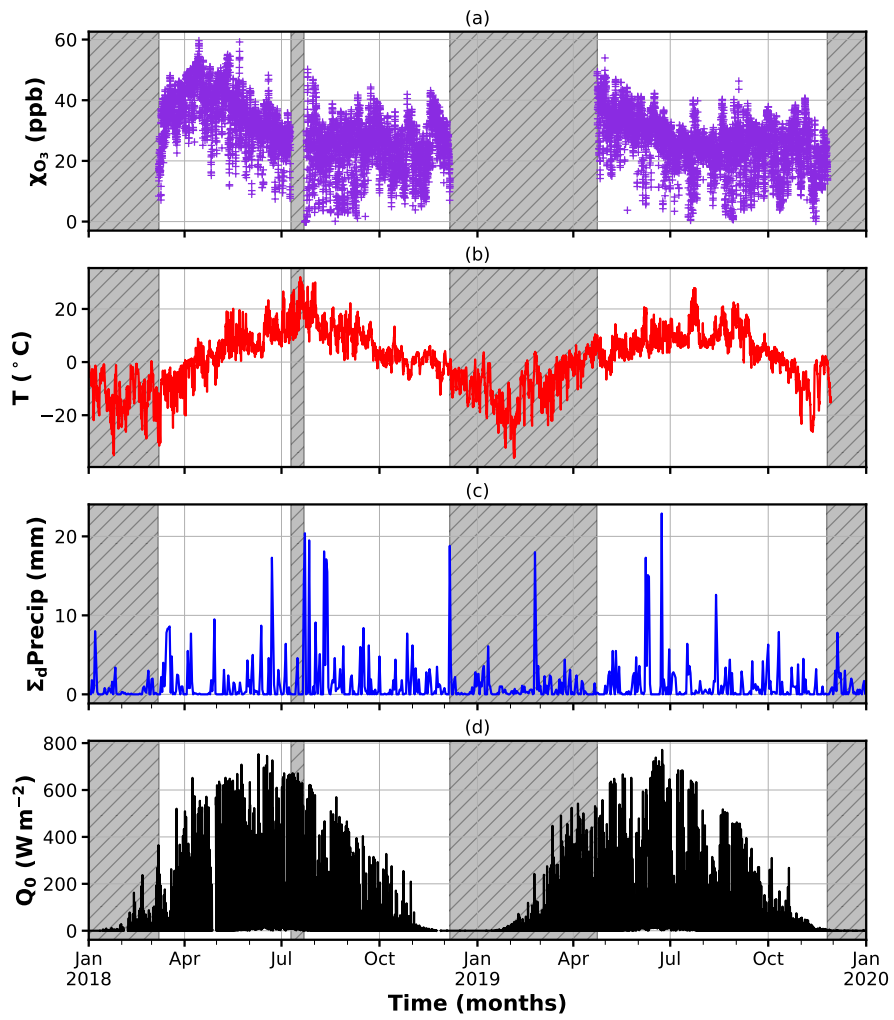


Figure 5. Observational data from atmospheric monitoring at Svanhovd in 2018/19. The hatched areas indicate periods without ozone monitoring data. (a) Hourly averaged ozone VMR; (b) hourly averaged temperature; (c) daily accumulated precipitation; (d) hourly averaged global irradiance.

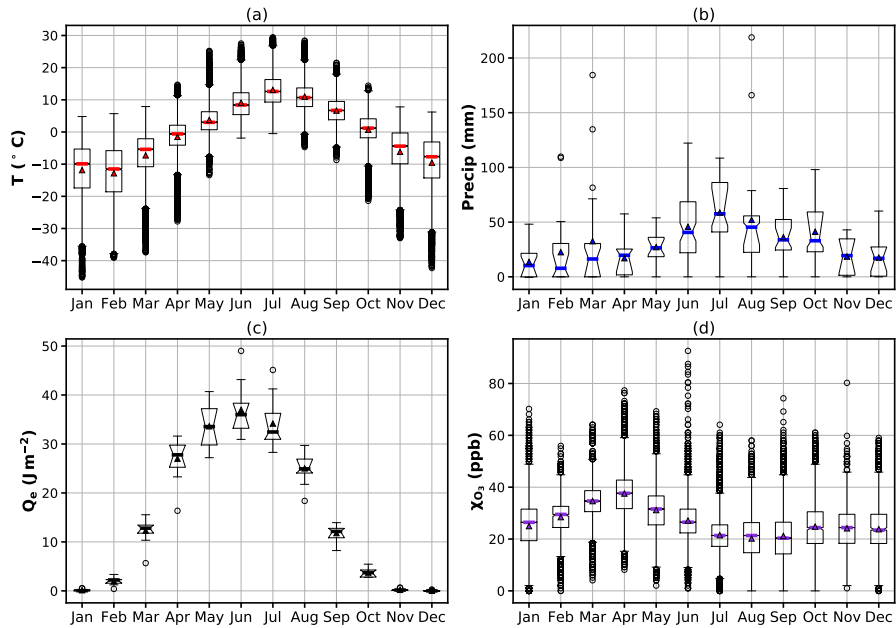


Figure 6. Climate diagram based on meteorological data for Svanvik/Pasvik (1992–2012). Ozone climatology based on ozone monitoring data (1986–1996). A box indicates the upper/lower quartile, whiskers the $1.5 \times$ Interquartile Range (IQR), and circles outliers. The median is marked by a colored horizontal line and the mean by a triangle. Notches indicate the confidence interval around the median. (a) Temperature; (b) accumulated precipitation; (c) radiant energy; (d) ozone VMR

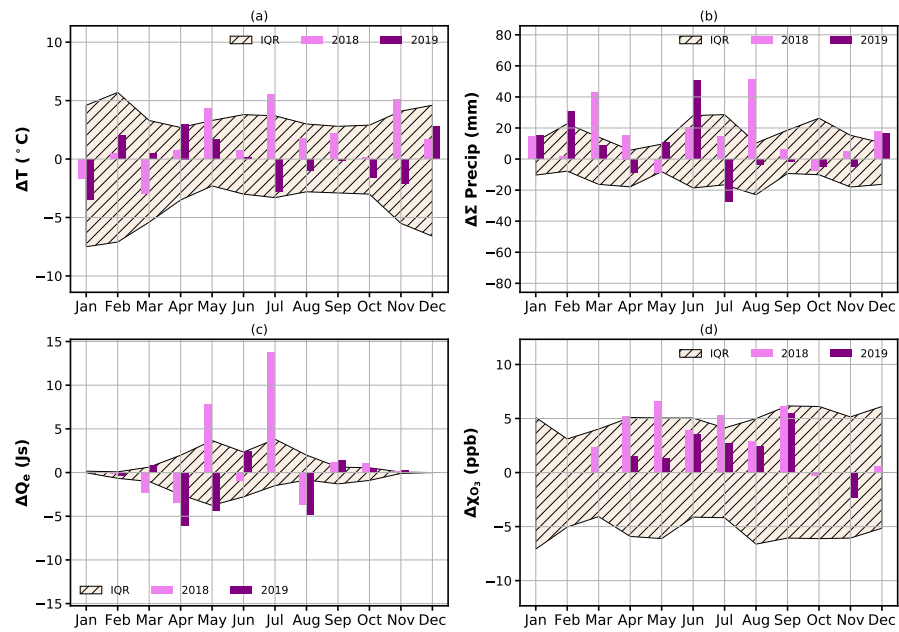


Figure 7. 2018/19 anomalies of key environmental variables at Svanhovd displayed as difference from median for each month. The hatched area between indicates the IQR. (a) Temperature; (b) precipitation; (c) radiant energy; (d) ozone VMR.

Appendix A: Growing season

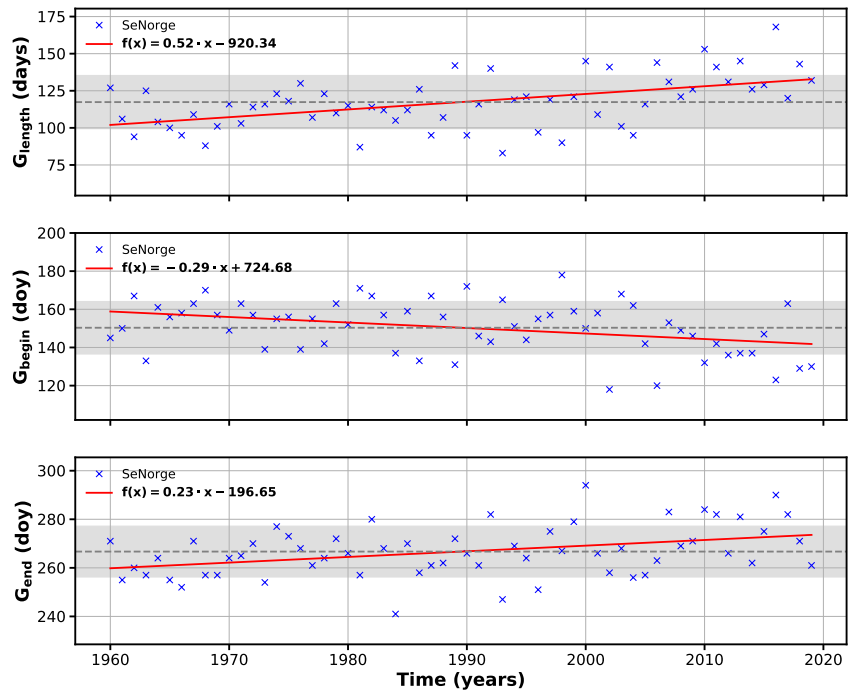


Figure A1. Estimated shift and prolongation of growing season at Svanhovd over the past 6 decades based on gridded observational temperature data from NVE, Meteorologisk Institutt, Kartverket (2020).

540 Appendix B: DO₃SE model

B1 Initial DO₃SE modeling results with mapping manual parameters

To demonstrate the necessary localization of the mapping manual parameters, we show the initial results of stomatal conductance at leaf-level ($G_{\text{sto}}^{\text{leaf}}$) and POD_y over doy for both years and all PFTs (Fig. B1). Observed χ_{O_3} is also indicated.

B2 Localized parameterizations

- 545 To assess the G_{start} and G_{end} of the growing season for coniferous trees at Svanhovd in 2018/19, we used the gross photosynthesis product (GPP) of MODIS AQUA/TERRA over a 1×1 km area centered at Svanhovd. MODIS data indicate a higher photosynthetic activity in 2018 than in 2019. As shown in Fig. B2, we fitted a second order polynomial function of the general

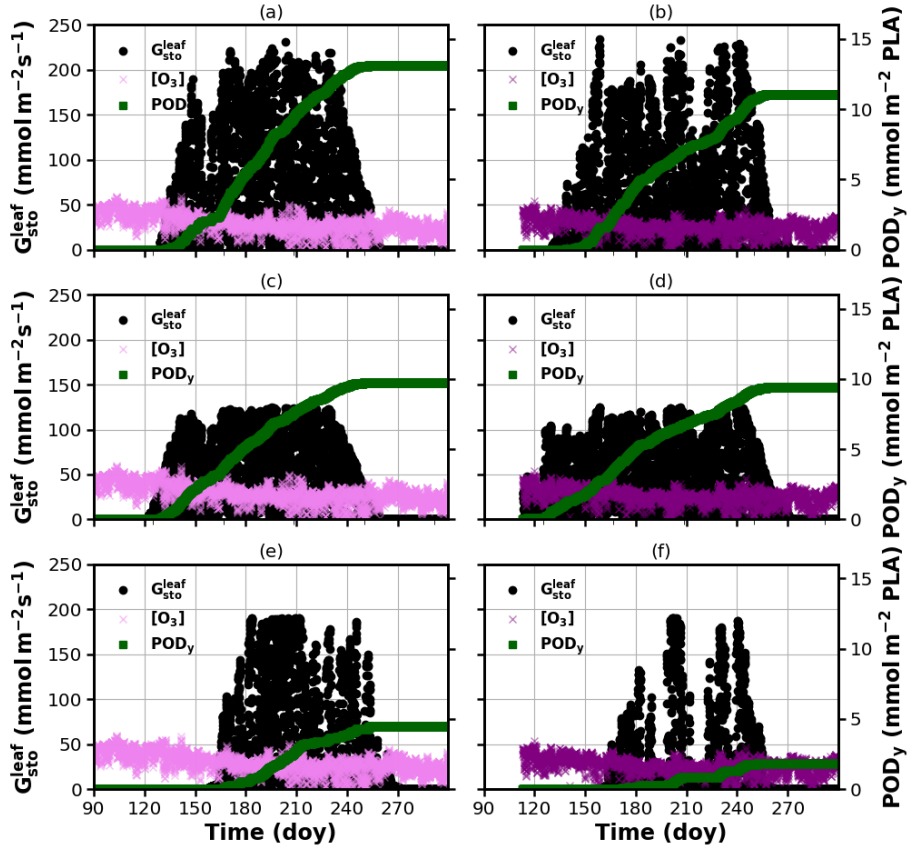


Figure B1. DO₃SE modeling results for mapping manual default parameterization. POD_y is shown over doy, March–October. A flux threshold $y = 1 \text{ nmol m}^{-2} \text{ s}^{-1}$ per projected leaf area (PLA) has been chosen. χ_{O_3} are plotted on the same axis and scales as $G^{\text{leaf}}_{\text{sto}}$ but in units of ppb. (a, b) deciduous tree; (c, d) coniferous tree; (e, f) perennial grassland. From left to right: 2018, 2019.

form

$$A_{\text{net}}(t) = -m_0 \cdot (t - m_1)^2 + m_2, \quad (\text{B1})$$

550 with the form parameters m_i to the data. Numerically, we retrieved the roots as $G_{\text{start}} = 122/106$ and $G_{\text{end}} = 261/274$ for 2018 and 2019, respectively.

Here, we show the temperature and light response functions for coniferous and deciduous trees (Figs. B3-B4).

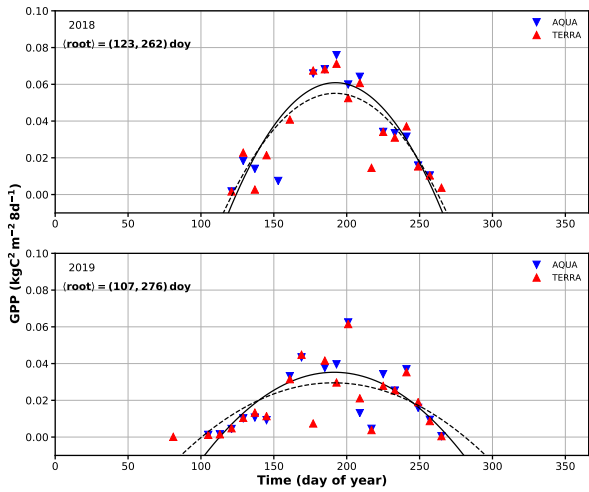


Figure B2. Estimated G_{start} and G_{end} of growing season for coniferous trees from MODIS Aqua/Terra gross primary productivity (GPP) product. A 1×1 km area around Svanhovd was selected. Daily averaged data for both 2018 and 2019 has been fitted with a quadratic polynomial function.

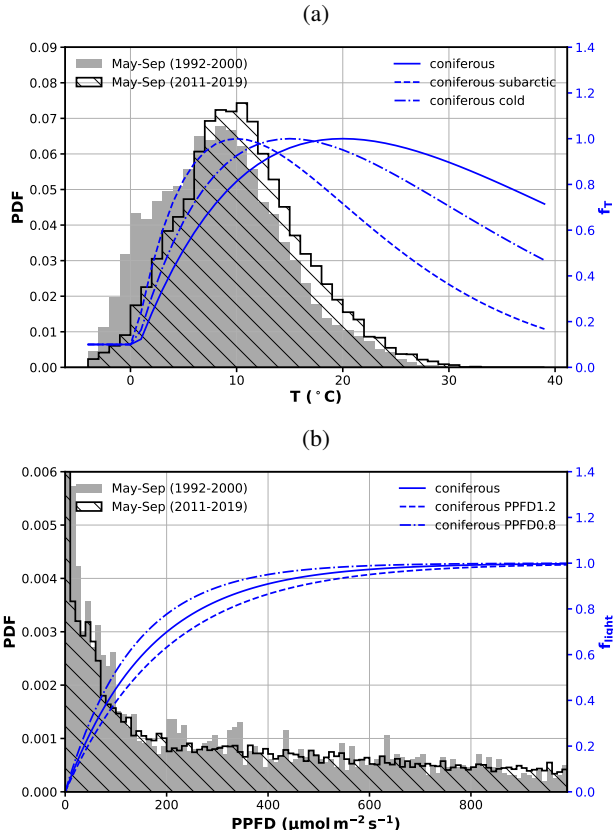


Figure B3. Construction of localized response functions for coniferous trees. (a) f_T and (b) f_{light} are shown together with underlying T_{air} and Q_0 climatologies (probability density function - PDF), respectively. Original mapping manual parameterization is shown in comparison as solid line. Note that the y-axis has been truncated to 0.006. PPFD0.8 and PPFD1.2 refer to α values increasing/decreasing PPFD at $f_{\text{light}} = 0.5$ by $\pm 20\%$, respectively.

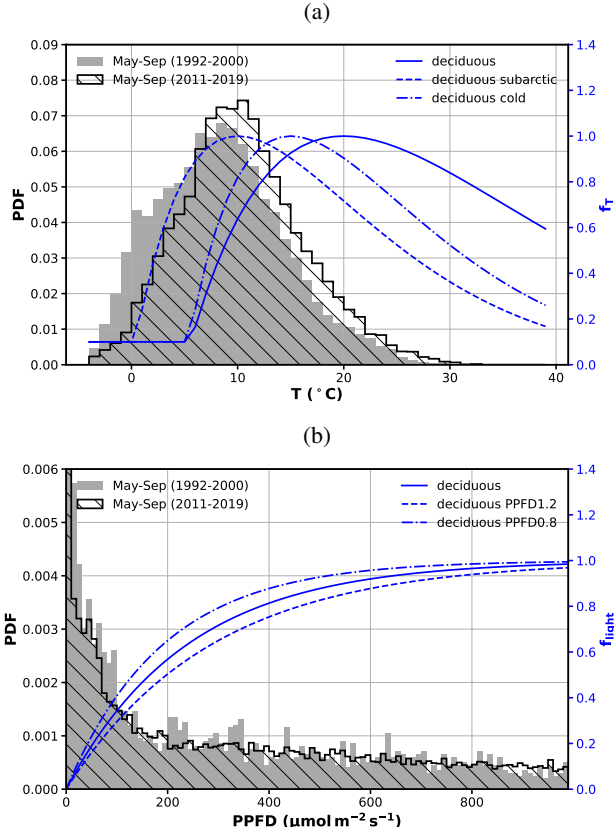


Figure B4. Construction of bespoke response functions for deciduous trees. (a) f_T and (b) f_{light} are shown together with underlying T_{air} and Q_0 climatologies (probability density function - PDF), respectively. Original mapping manual parameterization is shown in comparison as solid line. Note that Q_0 has been truncated to 0.006. PPFD0.8 and PPFD1.2 refer to α values increasing/decreasing PPFD at $f_{\text{light}} = 0.5$ by $\pm 20\%$, respectively.

Author contributions. All authors contributed to conceptualization of this research article and commented on the manuscript. SF has prepared the original draft, collected and processed ozone and environmental data, and performed all statistical analyses. AVV has conducted the on-site observation of vegetation damage induced by ozone, provided advice on plant physiological processes, collected existing literature on subarctic vegetation, contributed significantly proofreading this research article. LE has contributed with expertise in DO₃SE modeling and suggestion of the PDF-based temperature acclimation methodology. CO has collected PFT parameters from the literature, performed all DO₃SE simulations and validation. AE contributed with her experience regarding subarctic vegetation in Finnmark. FS contributed with an assessment of the 2018 meteorological conditions. TB gave valuable guidance in a broader research sense. Funding acquisition for the project: AVV, AE, FS, TB.

Competing interests. The authors declare that they have no conflict of interest.

Acknowledgements. We thank NILU for performing the ozone measurements at Svanhovd for us, Bjørg Rognerud (Department of Geosciences, UiO) for processing SeNorge.no data with respect to the beginning of the growing season, Tore Flatlandsmo Berglen (NILU) for hourly pressure data from Svanhovd, NIBIO Environment Center Svanhovd for establishing and running the ozone garden both years, and Volkmar Timmermann (NIBIO) for sharing ICP Forest data from Svanhovd. This work was supported by the Research Council of Norway (Grant No. 268073).

References

- Ainsworth, E. A.: Understanding and improving global crop response to ozone pollution, *Plant J.*, 90, 886–897, <https://doi.org/10.1111/tpj.13298>, 2017.
- 570 AMAP - Arctic Monitoring and Assessment Programme: Arctic Climate Issues 2011: Changes in Arctic Snow, Water, Ice and Permafrost, SWIPA 2011 Overview Report, Oslo, 978-82-7971-073-8, 2012.
- Andersson, C., Alpfjord, H., Robertson, L., Karlsson, P. E., and Engardt, M.: Reanalysis of and attribution to near-surface ozone concentrations in Sweden during 1990–2013, *Atmospheric Chemistry and Physics*, 17, 13 869–13 890, <https://doi.org/10.5194/acp-17-13869-2017>, 2017.
- 575 Ball, J., Woodrow, I., and Berry, J.: Progress in Photosynthesis Research, chap. A Model Predicting Stomatal Conductance and its Contribution to the Control of Photosynthesis under Different Environmental Conditions, Springer, Dordrecht, https://doi.org/10.1007/978-94-017-0519-6_48, 1987.
- Bassin, S., Kölliker, R., Cretton, C., Bertossa, M., Widmer, F., Bungener, P., and Fuhrer, J.: Intra-specific variability of ozone sensitivity in *Centaurea jacea* L., a potential bioindicator for elevated ozone concentrations, *Environ. Pollut.*, 131, 1–12, 580 <https://doi.org/10.1016/j.envpol.2004.02.014>, 2004.
- Beck, H., Zimmermann, N., McVicar, T., Vergopolan, N., Berg, A., and Wood, E.: Present and future Köppen-Geiger climate classification maps at 1-km resolution, *Sci. Data*, 5, 180 214, <https://doi.org/10.1038/sdata.2018.214>, 2018.
- Björklund, J.-Å., Ekelund, K., Henningsson, A., Perers, K., Peters, J., Siverstig, A., Uddholm, L.-G., and Wisén, J.: Betänkande av 2018 års skogsbrandsutredning, SOU2019 7, Statens Offentliga Utredningar (SOU), <https://www.regeringen.se/rattsliga-dokument/statens-offentliga-utredningar/2019/02/sou-20197/>, last accessed April 2020, 2019.
- 585 Buck, A. L.: New Equations for Computing Vapor Pressure and Enhancement Factor, *J. Appl. Meteorol.*, 20, 1527–1532, [https://doi.org/10.1175/1520-0450\(1981\)020<1527:NEFCVP>2.0.CO;2](https://doi.org/10.1175/1520-0450(1981)020<1527:NEFCVP>2.0.CO;2), 1981.
- Buck Research Instruments, LLC: Buck Research CR-1A User's Manual, Buck Research Instruments, LLC, PO Box 19498 Boulder, CO 80308, Appendix 1, 2012.
- 590 Büker, P., Morrissey, T., Briolat, A., Falk, R., Simpson, D., Tuovinen, J.-P., Alonso, R., Barth, S., Baumgarten, M., Grulke, N., Karlsson, P., King, J., Lagergren, F., Matyssek, R., Nunn, A., Ogaya, R., Penuelas, J., Rhea, L., Schaub, M., and Emberson, L.: DO3SE modelling of soil moisture to determine ozone flux to European forest trees, *Atmos. Chem. Phys.*, 12, 5537–5562, <https://doi.org/10.5194/acp-12-5537-2012>, 2012.
- 595 Clifton, O., Fiore, A., Massman, W., Baublitz, C., Coyle, M., Emberson, L., Fares, S., Farmer, D., Gentine, P., Gerosa, G., Guenther, A., Helmig, D., Lombardozzi, D., Munger, J., Patton, E., Pusede, S., Schwede, D., Silva, S., Sörgel, M., and Tai, A.: Dry Deposition of Ozone Over Land: Processes, Measurement, and Modeling, *Reviews of Geophysics*, p. e2019RG000670, <https://doi.org/10.1029/2019RG000670>, 2020.
- Cooper, O., Parrish, D., Ziemke, J., Balashov, N., Cupeiro, M., Galbally, I., Gilge, S., Horowitz, L., Jensen, N., Lamarque, J.-F., Naik, V., Oltmans, S., Schwab, J., Shindell, D., Thompson, A., Thouret, V., Wang, Y., and Zbinden, R.: Global distribution and trends of tropospheric ozone: An observation-based review, *Elementa-Sci Anthropol.*, 2, 000 029, <https://doi.org/10.12952/journal.elementa.000029>, 2014.
- 600 Derwent, R. G., Parrish, D. D., Galbally, I. E., Stevenson, D. S., Doherty, R. M., Naik, V., and Young, P. J.: Uncertainties in models of tropospheric ozone based on Monte Carlo analysis: Tropospheric ozone burdens, atmospheric lifetimes and surface distributions, *Atmos. Environ.*, 180, 93–102, <https://doi.org/10.1016/j.atmosenv.2018.02.047>, 2018.

605 https://www.dsbo.no/rapporter-og-evalueringer/skogbrannsesongen-2018/, 2019.

Emberson, L.: Effects of ozone on agriculture, forests and grasslands, Philosophical transactions. Series A, Mathematical, physical, and engineering sciences, 378, 20190 327, https://doi.org/10.1098/rsta.2019.0327, 2020.

610 Emberson, L. D., for Monitoring, C. P., of the Long Range Transmission of Air Pollutants in Europe, E., meteorologiske institutt, N., and Meteorological Synthesizing Centre-West (Oslo, N.: Towards a Model of Ozone Deposition and Stomatal Uptake Over Europe, EMEP/MSC-W Note, Norwegian Meteorological Institute, https://books.google.no/books?id=hj_ntgAACAAJ, last accessed May 2019, 2000.

Falk, S., Vollsnes, A. V., Eriksen, A. B., Stordal, F., and Koren Berntsen, T.: Technical note: Quality assessment of ozone reanalysis products and gap-filling over subarctic Europe for vegetation risk mapping, Atmos. Chem. Phys., 21, 15 647–15 661, https://doi.org/10.5194/acp-21-15647-2021, 2021.

615 Felzer, B. S., Cronin, T., Reilly, J. M., Melillo, J. M., and Wang, X.: Impacts of ozone on trees and crops, Comptes Rendus Geoscience, 339, 784–798, https://doi.org/https://doi.org/10.1016/j.crte.2007.08.008, 2007.

Fleming, Z. L., Doherty, R. M., von Schneidemesser, E., Malley, C. S., Cooper, O. R., Pinto, J. P., Colette, A., Xu, X., Simpson, D., Schultz, M. G., Lefohn, A. S., Hamad, S., Moolla, R., Solberg, S., and Feng, Z.: Tropospheric Ozone Assessment Report: Present-day ozone distribution and trends relevant to human health, Elementa-Sci Anthropol., 6, https://doi.org/10.1525/elementa.273, 2018.

620 Gangstø Skaland, R., Colleuille, H., Håvelsrød Andersen, A. S., Mamen, J., Grinde, L., Tajet, H. T. T., Lundstad, E., Sidselrud, L. F., Tunheim, K., Hanssen-Bauer, I., Benestad, R., Heiberg, H., and Hygen, H. O.: Tørkesommeren 2018, METinfo 14, Norwegian Meteorological Institute, https://www.met.no/publikasjoner/met-info/met-info-2019, last accessed March 2020, 2019.

625 Gaudel, A., Cooper, O. R., Ancellet, G., Barret, B., Boynard, A., Burrows, J. P., Clerbaux, C., Coheur, P. F., Cuesta, J., Cuevas, E., Doniki, S., Dufour, G., Ebojie, F., Foret, G., Garcia, O., Granados-Munoz, M. J., Hannigan, J. W., Hase, F., Hassler, B., Huang, G., Hurtmans, D., Jaffe, D., Jones, N., Kalabokas, P., Kerridge, B., Kulawik, S., Latter, B., Leblanc, T., Le Flochmoen, E., Lin, W., Liu, J., Liu, X., Mahieu, E., McClure-Begley, A., Neu, J. L., Osman, M., Palm, M., Petetin, H., Petropavlovskikh, I., Querel, R., Rahpoe, N., Rozanov, A., Schultz, M. G., Schwab, J., Siddans, R., Smale, D., Steinbacher, M., Tanimoto, H., Tarasick, D. W., Thouret, V., Thompson, A. M., Trickl, T., Weatherhead, E., Wespes, C., Worden, H. M., Vigouroux, C., Xu, X., Zeng, G., and Ziemke, J.: Tropospheric Ozone Assessment Report: Present-day distribution and trends of tropospheric ozone relevant to climate and global atmospheric chemistry model evaluation, Elementa-Sci Anthropol., 6, https://doi.org/10.1525/elementa.291, 2018.

Ghimire, R. P., Silfver, T., Myller, K., Oksanen, E., Holopainen, J. K., and Mikola, J.: BVOC Emissions From a Subarctic Ecosystem, as Controlled by Insect Herbivore Pressure and Temperature, Ecosystems, p. 20, https://doi.org/10.1007/s10021-021-00690-0, 2021.

Girgždienė, R., Serafinavičiūtė, B., Stakėnas, V., and Byčenkiene, S.: Ambient Ozone Concentration and its Impact on Forest Vegetation in Lithuania, AMBIO A Journal of the Human Environment, pp. 432–436, https://doi.org/10.1579/0044-7447-38.8.432, 2009.

635 Hartmann, D., Klein Tank, A., Rusticucci, M., Alexander, L., Broennimann, S., Charabi, Y., Dentener, F., Dlugokencky, E., Easterling, D., Kaplan, A., Soden, B., Thorne, P., Wild, M., and Zhai, P.: Observations: Atmosphere and Surface, book section 2, p. 159–254, Cambridge University Press, Cambridge, United Kingdom and New York, NY, USA, https://doi.org/10.1017/CBO9781107415324.008, 2013.

Hayes, F., Harmens, H., Mills, G., Bender, J., and Grünhage, L.: Ozone critical levels for (semi-)natural vegetation dominated by perennial grassland species, Environ. Sci. Pollut. Res., 28, 15 090–15 098, https://doi.org/10.1007/s11356-020-11724-w, 2021.

640 Høgda, K., Tømmervik, H., and Karlsen, S.: Trends in the Start of the Growing Season in Fennoscandia 1982–2011, Remote Sens., 5, 4304–4318, https://doi.org/10.3390/rs5094304, 2013.

- Høgda, K., Karlsen, S., and Solheim, I.: Climatic change impact on growing season in Fennoscandia studied by a time series of NOAA AVHRR NDVI data, in: IGARSS 2001. Scanning the Present and Resolving the Future. Proceedings. IEEE 2001 International Geoscience and Remote Sensing Symposium (Cat. No.01CH37217), vol. 3, pp. 1338–1340, <https://doi.org/10.1109/IGARSS.2001.976837>, 2001.
- 645 Jacobs, D. J., S.-M-Fa, Wofsy, S. C., Spiro, P. A., and Bakwin, P. S.: Deposition of Ozone to Tundra, *J. Geophys. Res.*, 97, 9, 1992.
- Jarvis, P. G.: The interpretation of the variations in leaf water potential and stomatal conductance found in canopies in the field, *Philos. T. Roy. Soc. B.*, 273, 593–610, <https://doi.org/10.1098/rstb.1976.0035>, 1976.
- Kangaskärvi, J., Jaspers, P., and Kollist, H.: Signalling and cell death in ozone-exposed plants, *Plant, Cell & Environment*, 28, 1021–1036, <https://doi.org/10.1111/j.1365-3040.2005.01325.x>, 2005.
- 650 Karlsen, S., Solheim, I., Beck, P., Høgda, K., Wielgolaski, F., and Tømmervik, H.: Variability of the start of the growing season in Fennoscandia, 1982–2002, *Int. J. Biometeorol.*, 51, 513–24, <https://doi.org/10.1007/s00484-007-0091-x>, 2007.
- Karlsson, P., Tang, L., Klingberg, J., Chen, D., Lindskog, A., and Pleijel, H.: Increasing risk for negative ozone impacts on vegetation in northern Sweden, *Environ. Pollut.*, 150, 96–106, <https://doi.org/10.1016/j.envpol.2007.06.016>, 2007.
- Karlsson, P., Ferm, M., Tømmervik, H., Hole, L., Karlsson, G., Ruoho-Airola, T., Aas, W., Hellsten, S., Akselsson, C., Mikkelsen, T., and 655 Nihlgård, B.: Biomass burning in eastern Europe during spring 2006 caused high deposition of ammonium in northern Fennoscandia, *Environ. Pollut.*, 176C, 71–79, <https://doi.org/10.1016/j.envpol.2012.12.006>, 2013.
- Karlsson, P. E., Pihl Karlsson, G., and Pleijel, H.: En förbättrad metodik för att beräkna ozonkänsliga perioder för växtligheten under året, Tech. rep., IVL Svenska Miljöinstitutet, <https://gup.ub.gu.se/publication/273605>, 2018.
- 660 Keronen, P., Reissell, A., Üllar Rannik, Pohja, T., Siivola, E., Hiltunen, V., Hari, P., Kulmala, M., and Vesala, T.: Ozone flux measurements over a Scots pine forest using eddy covariance method: performance evaluation and comparison with flux-profile method, *BOREAL ENVIRONMENT RESEARCH*, 8, 425–443, 2003.
- Klingberg, J., Björkman, M., Karlsson, G., and Pleijel, H.: Observations of Ground-level Ozone and NO₂ in Northernmost Sweden, Including the Scandian Mountain Range, *AMBIO*, 38, 448–451, <https://doi.org/10.1579/0044-7447-38.8.448>, 2009.
- Klingberg, J., Karlsson, P. E., Andersson, C., Engardt, M., Karlsson, G. P., and Pleijel, H.: Observed annual surface ozone maxima and 665 minima in northern and central Europe from 1990–2015 – latitude dependence and temporal trends, *Boreal Environ. Res.*, 24, 201–214, 2019.
- Kolari, P., Lappalainen, H., Hänninen, H., and Hari, P.: Relationship between temperature and the seasonal course of photosynthesis in Scots pine at northern timberline and in southern boreal zone, *Tellus B*, 59, 542–552, <https://doi.org/10.3402/tellusb.v59i3.17033>, 2007.
- Korhonen, P., Palosuo, T., Persson, T., Höglind, M., Jégo, G., Van Oijen, M., Gustavsson, A.-M., Bélanger, G., and Virkajarvi, P.: 670 Modelling grass yields in northern climates – a comparison of three growth models for timothy, *Field Crops Research*, 224, 37–47, <https://doi.org/10.1016/j.fcr.2018.04.014>, 2018.
- Lawrence, D. M., Fisher, R. A., Koven, C. D., Oleson, K. W., Swenson, S. C., Bonan, G., Collier, N., Ghimire, B., van Kampenhout, L., Kennedy, D., Kluzek, E., Lawrence, P. J., Li, F., Li, H., Lombardozzi, D., Riley, W. J., Sacks, W. J., Shi, M., Vertenstein, M., Wieder, W. R., Xu, C., Ali, A. A., Badger, A. M., Bisht, G., van den Broeke, M., Brunke, M. A., Burns, S. P., Buzan, J., Clark, M., Craig, A., Dahlin, K., 675 Drewniak, B., Fisher, J. B., Flanner, M., Fox, A. M., Gentine, P., Hoffman, F., Keppel-Aleks, G., Knox, R., Kumar, S., Lenaerts, J., Leung, L. R., Lipscomb, W. H., Lu, Y., Pandey, A., Pelletier, J. D., Perket, J., Randerson, J. T., Ricciuto, D. M., Sanderson, B. M., Slater, A., Subin, Z. M., Tang, J., Thomas, R. Q., Val Martin, M., and Zeng, X.: The Community Land Model Version 5: Description of New Features, Benchmarking, and Impact of Forcing Uncertainty, *J. Adv. Model. Earth Syst.*, 11, 4245–4287, <https://doi.org/10.1029/2018MS001583>, 2019.

- 680 Lin, M., Horowitz, L., Xie, Y., Paulot, F., Malyshev, S., Shevliakova, E., Finco, A., Gerosa, G., Kubistin, D., and Pilegaard, K.: Vegetation feedbacks during drought exacerbate ozone air pollution extremes in Europe, *Nat. Clim. Change*, 10, 444–451, <https://doi.org/10.1038/s41558-020-0743-y>, 2020.
- Lindskog, A., Karlsson, P., Grennfelt, P., Solberg, S., and Forster, C.: An exceptional ozone episode in northern Fennoscandia, *Atmos. Environ.*, 41, 950–958, <https://doi.org/10.1016/j.atmosenv.2006.09.027>, 2007.
- 685 Lombardozzi, D., Sparks, J. P., and Bonan, G.: Integrating O₃ influences on terrestrial processes: photosynthetic and stomatal response data available for regional and global modeling, *Biogeosciences*, 10, 6815–6831, <https://doi.org/10.5194/bg-10-6815-2013>, 2013.
- Maas, R., grennfelt, p., Amann, M., Harnett, B., Kerr, J., Berton, E., Pritula, D., Reiss, I., Almodovar, P., Héroux, M.-E., Fowler, D., Wright, D., de Wit, H., Tørseth, K., Mareckova, K., LeGall, A.-C., Rabago, I., Hettelingh, J.-P., Haeuber, R., and Reis, S.: Towards Cleaner Air. Scientific Assessment Report 2016, UN ECE, 2016.
- 690 Manninen, S., Huttunen, S., Tømmervik, H., Hole, L. R., and Solberg, S.: Northern Plants and Ozone, *AMBIO: A Journal of the Human Environment*, 38, 406 – 413, <https://doi.org/10.1579/0044-7447-38.8.406>, 2009.
- Matyssek, R., Wieser, G., Calfapietra, C., de Vries, W., Dizengremel, P., Ernst, D., Jolivet, Y., Mikkelsen, T. N., Mohren, G. M. J., Le Thiec, D., Tuovinen, J. P., Weatherall, A., and Paoletti, E.: Forests under climate change and air pollution: Gaps in understanding and future directions for research, *Environ. Pollut.*, 160, 57–65, <https://doi.org/10.1016/j.envpol.2011.07.007>, 2012.
- 695 Medlyn, B. E., Duursma, R. A., Eamus, D., Ellsworth, D. S., Prentice, I. C., Barton, C. V. M., Crous, K. Y., de Angelis, P., Freeman, M., and Wingate, L.: Reconciling the optimal and empirical approaches to modelling stomatal conductance, *Glob. Change Biol.*, 17, 2134–2144, <https://doi.org/10.1111/j.1365-2486.2010.02375.x>, 2011.
- Menzel, A., Sparks, T., Estrella, N., Koch, E., Aasa, A., Ahas, R., Alm-Kübler, K., Bissolli, P., Braslavská, O., Briede, A., Chmielewski, F., Črepinské, Z., Curnel, Y., Defila, C., Donnelly, A., Filella, I., Jatczak, K., Måge, F., and Zist, A.: European phenological response 700 to climate change matches the warming pattern, *Glob. Change Biol.*, 12, 1969–1976, <https://doi.org/10.1111/j.1365-2486.2006.01193.x>, 2006.
- Mills, G., Hayes, F., Simpson, D., Emberson, L., Norris, D., Harmens, H., and Büker, P.: Evidence of widespread effects of ozone on crops and (semi-)natural vegetation in Europe (1990–2006) in relation to AOT40- and flux-based risk maps, *Glob. Change Biol.*, 17, 592 – 613, <https://doi.org/10.1111/j.1365-2486.2010.02217.x>, 2011.
- 705 Mills, G., Harmens, H., Hayes, F., Pleijel, H., Büker, P., González-Fernández, I., Alonso, R., Bender, J., Bergmann, E., Bermejo, V., Braun, S., Danielsson, H., Gerosa, G., Grünhage, L., Karlsson, P. E., Marzuoli, R., Schaub, M., and Simpson, D.: ICP Mapping Manual - Chapter III: Mapping Critical Levels for Vegetation, International Cooperative Programme on Effects of Air Pollution on Natural Vegetation and Crops, https://www.umweltbundesamt.de/en/Coordination_Centre_for_Effects, minor edits OCT 2017, last accessed Feb 2019, 2017.
- Mills, G., Pleijel, H., Malley, C. S., Sinha, B., Cooper, O. R., Schultz, M. G., Neufeld, H. S., Simpson, D., Sharps, K., Feng, Z., Gerosa, 710 G., Harmens, H., Kobayashi, K., Saxena, P., Paoletti, E., Sinha, V., and Xu, X.: Tropospheric Ozone Assessment Report: Present-day tropospheric ozone distribution and trends relevant to vegetation, *Elementa-Sci Anthropol.*, 6, <https://doi.org/10.1525/elementa.302>, 2018.
- Musselman, R. C., Lefohn, A. S., Massman, W. J., and Heath, R. L.: A critical review and analysis of the use of exposure- and flux-based ozone indices for predicting vegetation effects, *Atmos. Environ.*, 40, 1869–1888, <https://doi.org/10.1016/j.atmosenv.2005.10.064>, 2006.
- NIBIO: LandbruksMeteorologisk Tjeneste, <https://lmt.nibio.no/>, last accessed July 2020.
- 715 NVE, Meteorologisk Institutt, Kartverket: SeNorge.no, online, <http://www.senorge.no>, last accessed April 2020, 2020.
- Padro, J.: Summary of ozone dry deposition velocity measurements and model estimates over vineyard, cotton, grass and deciduous forest in summer, *Atmo. Environ.*, 30, 7, 1996.

Peñuelas, J. and Llusià, J.: BVOCs: plant defense against climate warming?, *Trends Plant Sci.*, 8, 105–109, [https://doi.org/10.1016/S1360-1385\(03\)00008-6](https://doi.org/10.1016/S1360-1385(03)00008-6), 2003.

720 Poulter, B., MacBean, N., Hartley, A., Khlystova, I., Arino, O., Betts, R., Bontemps, S., Boettcher, M., Brockmann, C., Defourny, P., Hagemann, S., Herold, M., Kirches, G., Lamarche, C., Lederer, D., Ottle, C., Peters, M., and Peylin, P.: Plant functional type classification for earth system models: results from the European Space Agency's Land Cover Climate Change Initiative, *Geosci. Model Dev.*, 8, 2315–2328, <https://doi.org/10.5194/gmd-8-2315-2015>, 2015.

Running, S., Mu, Q., and Zhao, M.: MYD17A2H MODIS/Aqua Gross Primary Productivity 8-Day L4 Global 500m SIN Grid V006, 725 <https://doi.org/10.5067/MODIS/MYD17A2H.006>, accessed 2020-08-03, 2015.

Shutova, E., Wielgolaski, F., Karlsen, S., Makarova, O., Berlin, N., Filimonova, A., Haraldsson, E., Aspholm, P. E., Flø, L., and Høgda, K. A.: Growing seasons of Nordic mountain birch in northernmost Europe as indicated by long-term field studies and analyses of satellite images, *Int. J. Biometeorol.*, pp. 155–166, <https://doi.org/10.1007/s00484-006-0042-y>, 2006.

730 Simpson, D., Ashmore, M., Emberson, L., and Tuovinen, J.-P.: A comparison of two different approaches for mapping potential ozone damage to vegetation. A model study, *Environ. Pollut.*, 146, 715–725, <https://doi.org/10.1016/j.envpol.2006.04.013>, critical Levels for Ozone Effects on Vegetation: Further Applying and Developing the Flux Concept, 2007.

Simpson, D., Tuovinen, J. P., Emberson, L., and Ashmore, M. R.: Characteristics of an ozone deposition module II: Sensitivity analysis, *Water Air Soil Poll.*, 143, 123–137, <https://doi.org/10.1023/A:1022890603066>, 2003.

735 Simpson, D., Benedictow, A., Berge, H., Bergstrom, R., Emberson, L., Fagerli, H., Flechard, C. R., Hayman, G. D., Gauss, M., Jonson, J. E., Jenkin, M. E., Nyiri, A., Richter, C., Semeena, V. S., Tsyró, S., Tuovinen, J.-P., Valdebenito, A., and Wind, P.: The EMEP MSC-W chemical transport model - technical description, *Atmos. Chem. Phys.*, 12, 7825–7865, <https://doi.org/10.5194/acp-12-7825-2012>, 2012.

Solberg, S.: Monitoring of boundary layer ozone in Norway from 1977 to 2002, Ozone Report 2003 85, Norwegian Institute for Air Research (NILU), 2003.

740 Solberg, S., Hov, Ø., Haslerud, A., Isaksen, S., Coddeville, P., De Backer, H., Forster, C., Orsolini, Y., and Uhse, K.: European surface ozone in the extreme summer 2003, *J. Geophys. Res.*, 113, 1–16, <https://doi.org/10.1029/2007JD009098>, 2008.

Systad, G. H., Strann, K.-B., and Frivoll, V.: Biologisk mangfold Sør-Varanger kommune, Nina oppdragsmelding, Norsk institutt for naturforskning (NINA), <https://www.nina.no/archive/nina/PppBasePdf/oppdragsmelding/829.pdf>, 2004.

Wallin, G., Hall, M., Slaney, M., Räntfors, M., Medhurst, J., and Linder, S.: Spring photosynthetic recovery of boreal Norway spruce under conditions of elevated [CO₂] and air temperature, *Tree Physiol.*, 33, <https://doi.org/10.1093/treephys/tpt066>, 2013.

745 Wesely, M. L.: Parameterization Of Surface Resistances To Gaseous Dry Deposition In Regional-Scale Numerical-Models, *Atmos. Environ.*, 23, 1293–1304, [https://doi.org/10.1016/0004-6981\(89\)90153-4](https://doi.org/10.1016/0004-6981(89)90153-4), 1989.

Wespé, C., Hurtmans, D., Clerbaux, C., Boynard, A., and Coheur, P.-F.: Decrease in tropospheric O₃ levels in the Northern Hemisphere observed by IASI, *Atmospheric Chemistry and Physics*, 18, 6867–6885, <https://doi.org/10.5194/acp-18-6867-2018>, 2018.

750 Wittig, V. E., Ainsworth, E. A., Naidu, S. L., Karnosky, D. F., and Long, S. P.: Quantifying the impact of current and future tropospheric ozone on tree biomass, growth, physiology and biochemistry: a quantitative meta-analysis, *Glob. Change Biol.*, 15, 396–424, <https://doi.org/10.1111/j.1365-2486.2008.01774.x>, 2009.